Contributions To Mineralogy And Petrology
October 2021, Volume 176 Issue 10 Pages 75 (24p.)
https://doi.org/10.1007/s00410-021-01833-1
https://archimer.ifremer.fr/doc/00722/83434/

Mantle xenolith-bearing phonolites and basanites feed the active volcanic ridge of Mayotte (Comoros archipelago, SW Indian Ocean)

Berthod Carole [1, *], Médard Etienne [1], Di Muro Andrea [2, 3], Hassen Ali Théo [1], Gurioli Lucia [1], Chauvel Catherine [3], Komorowski Jean-Christophe [3], Bachèlery Patrick [1], Peltier Aline [2, 3], Benbakkar Mhammed [1], Devidal Jean-Luc [1], Besson Pascale [3], Le Friant Anne [3], Deplus Christine [3], Nowak Sophie [3], Thinon Isabelle [4], Burckel Pierre [3], Hidalgo Samia [3], Feuillet Nathalie [3], Jorry Stephan [5], Fouquet Yves [5]

[1] Laboratoire Magmas et Volcans, Université Clermont Auvergne, CNRS, IRD, OPGC, Clermont-Ferrand, France
[2] Observatoire Volcanologique du Piton de la Fournaise, Institut de physique du globe de Paris, 97418, La Plaine des Cafres, France
[3] Institut de physique du globe de Paris, CNRS, Université de Paris, 75005, Paris, France
[4] BRGM, French Geological Survey, 3 avenue Claude Guillemin, BP36009, 45 060, Cédex 2, Orléans, France
[5] Ifremer, Unité Géosciences Marines, 29280, Plouzané, France

* Corresponding author : Carole Berthod, email address : carole.berthod@uca.fr

Abstract :

Since 2018, the submarine east flank of Mayotte Island (Comoros archipelago) is the site of a major eruption located at 3.5 km depth bsl on a WNW-ESE volcanic ridge. Samples brought by oceanographic cruises carried out to monitor this seismo-volcanic crisis indicate that this volcanic ridge is built by a bimodal sodic alkaline magmatic series that includes basanites and phonolites. A petrological study of dredged samples allowed us to image the magmatic system feeding the volcanic ridge and to determine the link between basanitic and phonolitic magmas. The magmatic system feeding the volcanic ridge comprises multiple levels of magma storage. Basanitic magmas generated at 80–100 km mantle depth are stored in two or more deep reservoirs (≥ 37 km) and then in shallower basanitic and phonolitic lenses located close to the Moho interface before rising the surface. This study identifies three possible scenarios: (1) the deep basanitic magma rises directly and quickly to the surface from the deep mantle reservoir (as is currently happening 60 km offshore), (2) the basanitic magma stalls in a shallower reservoir near the Moho before resuming its ascent toward the surface and erupting as porphyritic basanite, (3) the basanitic magma stops and evolves to phonolite in these sub-crustal reservoirs. The phonolitic lavas are produced by approximately 80% fractional crystallization (34% clinopyroxene, 30% anorthoclase feldspar, 15.5% magnetite, 12.5% olivine, 5% apatite and 4% ilmenite) of a hydrous basanitic magma at mantle depths (P > 0.6 GPa) under reduced oxygen fugacity (~ FMQ-1). In this third scenario, the phonolitic magma might be reactivated by the arrival of a new batch of deeper basanitic magma.

Keywords : Mayotte, Basanite, Phonolite, Magmatic system, Fractional crystallization

1. Introduction

The deepest part (3.5 km bsl) of the eastern submarine flank of Mayotte is the site of long lasting and still ongoing (as of January 2021) effusive volcanic activity that followed an intense volcano-tectonic crisis beginning in May 2018 (Berthod et al. 2021; Cesca et al. 2020; Feuillet et al. 2021; Lemoine et al. 2020). A series of oceanographic cruises organized by the French scientific community have led to the discovery of an active volcanic ridge characterized by basanitic and phonolitic volcanic cones and lava fields, and extending 60 km from the deep distal eruptive site to the subaerial easternmost part of Mayotte island, Petite Terre (Feuillet, 2019; Feuillet et al. 2021; Fouquet and Feuillet, 2019; Jorry, 2019). Both subaerial and submarine phonolitic eruptive products carry mm to dm sized ultramafic xenoliths testifying to rapid ascent from mantle levels. Worldwide, most phonolitic magmas evolve and reside in shallow crustal reservoirs (e.g., Scaillet et al. 2008; Grant et al. 2013; Moussallam et al. 2013), and mantle xenolith-bearing phonolites are extremely rare (Dautria et al., 1983; Grant et al. 2013; Price and Green, 1972). Phonolites usually result from fractional crystallization of a basanitic parental magma (Ablay et al. 1998; Kyle et al. 1992; Le roex et al. 1990), although phonolitic melts can be generated directly by mantle melting (Laporte et al. 2014). Berthod et al. (2021) demonstrate that lavas erupted in 2018-2019 from the distal submarine site are basanitic and ascended rapidly from a large deep reservoir located in the lithospheric mantle. Slight chemical evolution of the erupted lavas over time was interpreted as evidence of syn-eruptive mixing between the ascending basanite and a shallower, cooler and more differentiated magma possibly stored close to the Moho interface.

Long-standing activity on the Mayotte active volcanic ridge allows us to explore the origin of deep phonolites and their evolution at mantle level together with their link with the basanite volcanism. Are basanite and phonolites both primitive mantle melting products? Or do phonolites derive through fractional crystallization of the basanites? In order to answer these questions, we performed a detailed petrological and geochemical investigation, including petrological analysis, thermobarometry and *in situ* and whole-rock geochemistry of the submarine volcanic products collected along the Mayotte submarine ridge during three successive oceanographic cruises (MAYOBS 1, MAYOBS 2 and MAYOBS 4) between May and July 2019 (Feuillet, 2019; Feuillet et al. 2019; Fouquet and Feuillet, 2019; Jorry, 2019), and compared them with recent (Holocene) subaerial products collected during two field campaigns on Petite Terre in 2018 and 2019.

2. Geological setting

The Comoros Archipelago, located in the Mozambique Channel between the northern tip of Madagascar and the eastern coast of Mozambique (Fig. 1a) consists of four islands: Mayotte, Anjouan, Moheli and Grande Comore, from east to west. These islands are interconnected by a series of submarine volcanic ridges and are associated with atolls and partially emerged reef platforms (Tzevahirtzian et al. 2021). The overall archipelago has been recently interpreted as the NW-SE boundary between the Lwandle microplate and the Somalia plate, a boundary marked by a zone of active seismicity connecting the northern extremity of Madagascar in the east to the African coast in the west (Bertil and Regnoult, 1998; Dziewonski et al. 1981; Ekström et al. 2012; Famin et al. 2020). This boundary may consist of a zone of broad deformation extending up to the northern half of Madagascar (Stamps et al. 2021) or of a more localized dextral transfer zone between the offshore branch of the East-African rift and Madagascar (Famin et al. 2020; Feuillet et al. 2021).

The origin of Comorian volcanism is a long-lasting debate (Bachèlery and Hémond, 2016; Class et al., 2009; Claude-Ivanaj et al., 1998; Coltorti et al. 1999; Deniel, 1998a; Flower, 1973; Michon, 2016; Nougier et al. 1986; Pelleter et al. 2014; Strong, 1972; Thompson and Flower, 1971; Tzevahirtzian et al. 2021). According to the latest investigations, it is likely associated with lithospheric deformation possibly in relation to the East African Rift System (Courgeon et al. 2017; Lemoine et al. 2020; Michon, 2016; Nougier et al. 1986; Tzevahirtzian et al. 2021), rather than being the result of the interaction of a mantle plume with oceanic lithosphere (Class

et al. 2009, 2005, 1998; Class and Goldstein, 1997; Claude-Ivanaj et al. 1998; Deniel, 1998b; Emerick and Duncan, 1982; Hajash and Armstrong, 1972).

Mayotte, the easternmost part of the archipelago, is composed of a main volcanic island (Grande Terre) and a volcanic islet (Petite Terre), located 4 km east of Grande Terre and built on the modern barrier reef (Nehlig et al., 2013). Mayotte subaerial activity is subdivided into multiple phases of volcanism beginning in the southern part of Grande Terre (10.6 – 1.9 Ma) and then migrating toward the north (7.1 – 1 Ma) and the east (2.4 Ma – present) separated by periods of quiescence (Debeuf, 2004; Pelleter et al. 2014). Magmas emitted on Mayotte show a wider range of differentiation compared to the other islands of the Comoros archipelago, and they define two magmatic series ranging from strongly silica-undersaturated alkaline magmas in the older series to weakly alkaline magmas in the most recent ones (Fig. 2a).

Mayotte is considered the oldest island of Comoros archipelago with a maximum age of 20 Ma for the submarine onset of magmatic activity (Debeuf, 2004; Emerick and Duncan, 1982; Hajash and Armstrong, 1972; Michon, 2016; Nougier et al. 1986; Pelleter et al. 2014; Tzevahirtzian et al. 2021). Despite being the oldest island of the archipelago, Holocene volcanic activity has been documented both on land (Zinke et al. 2003) and on its submarine flanks. In May 2018, an intense seismo-volcanic crisis began on the distal part of a 60 km long NW-SE volcanic ridge that runs off the eastern submarine flank of Mayotte (Fig. 1b; Cesca et al. 2020; Lemoine et al. 2020). This WNW-ESE-oriented volcanic ridge extends from the site of the ongoing eruption in the east to Petite Terre Island in the west (Berthod et al. 2021; Feuillet et al. 2021), see Figure 1). Petite Terre is indeed characterized by the presence of very recent (200 to 4 ka; Zinke, (2003)) phonolitic phreatomagmatic activity with well-preserved maar structures, and strombolian mafic cones aligned on N140 oriented fractures. Strombolian mafic cones are also present in the lagoon between Grande Terre and Petite Terre.

The presence of these recent volcanic structures along the east coast of Mayotte and the ongoing submarine eruption on the east flank of the island raises the question of the possible triggering of a future volcanic activity on the island itself. Indeed, ongoing volcanic seismicity is not only present below the active volcano, 60 km from the island, but the most significant seismic activity is currently recorded 5 – 15 km offshore the island of Petite Terre and below the volcanic ridge (Lemoine et al. 2020; ReVoSiMa, 2021).

Our first petrological study was focused on the lavas erupted at the active volcanic site, which represent an evolved basanite endmember (Berthod et al. 2021). The goal of this study is to explore the most silicic (phonolite) endmember and the link between both endmembers to constrain the conditions of magma storage, evolution and ascent along the ridge. Our data

contribute to image the magmatic system feeding the volcanic ridge east of Mayotte and to constrain the possible future volcanic hazards all along the Mayotte volcanic ridge.

3. Methods

1.1. Samples and dredges

Samples from the active submarine volcanic ridge on the East flank of Mayotte Island were recovered from water depths ranging from 3,200 to 1,000 m by the *R/V Marion Dufresne* in May, June and July 2019, during oceanographic cruises MAYOBS 1, 2 and 4 (Feuillet, 2019; Fouquet and Feuillet, 2019; Jorry, 2019). In addition to those realized on the eruptive site (MAY01-DR01, MAY02-DR08, MAY04-DR10, MAY04-DR11 and MAY04-DR12, Fig. 1b, Berthod et al. 2021), dredges have been performed on four strategic sites identified from high-resolution bathymetric survey of the entire volcanic ridge (Fig. 1 and Tab. 1). The dredged samples were recovered in the proximal part, 10 – 15 km east of Petite Terre Island, on and near a site informally nicknamed "Horseshoe" due to the horseshoe-shape of the submarine volcanic feature (MAY01-DR02, MAY02-DR06, MAY02-DR07 and MAY04-DR09). Three dredges collected samples from individual volcanic cones (MAY01-DR02, MAY02-DR06 and MAY04-DR09). One dredge (MAY02-DR07), was performed on a highly reflective lava flow on the southeastern part of the Horseshoe site (Fig. 1b). Dredged samples were observed and described onboard. We selected unaltered samples with representative morphologies and textures, including quenched pillow rims, pillow cores, and samples containing xenoliths and crystals.

With the notable exception of MAY02-DR06, each dredge collected a very homogeneous set of rock types, *a priori* sampling the same volcanic unit. Individual volcanic cones sampled by dredges MAY02-DR06 and MAY04-DR09, are built from lavas characterized by the presence of a chilled margin (1 – 2 cm thick), and an inward increase in vesicle density. A few olivine and clinopyroxene crystals are observed in MAY02-DR06 and MAY04-DR09 samples. MAY01-DR02 and MAY02-DR07 samples display a glassy thick chilled margin (~ 4 cm), characterized by a rounded, cracked surface and sharp conchoidal fractures. The internal part presents a bedded aspect, which is delimited by elongated and flattened vesicles. These vesicles can reach several centimeters in length and are organized in the plane parallel to the surface of the sample. Importantly, this facies is also observed in some samples from the MAY02-DR06 dredge.

Samples collected on Petite Terre island are also used for comparison and include a phonolitic glassy sample from the Vigie maar (MAY181215-14b, surrounding a large ultramafic xenolith - MAY181215-14a) and a mafic crystal-rich lithic fragment from a phonolitic pyroclastic deposit at Moya maar (MAY181214-02) that represents the island's basement. Angular, decametric to centimetric mantle xenoliths are found in pyroclastic phonolitic deposits from la Vigie (MAY181215-14a, MAY190911-4a, MAY190911-4b, MAY190911-4c, MAY190911-4d) and Dziani (MAY190911-6a) phonolitic maars on Petite Terre. Smaller xenoliths (cm to mm-sized) are also found in the phonolitic lava flow sampled by dredge MAY02-DR07 (MAY02-DR070207E, MAY02-DR070208E).

1.2. Bulk-rock analysis

Bulk rock compositions were obtained on samples distributed between four dredges and two sampling sites on Petite Terre (Fig. 1b). Major elements were analyzed by ICP-AES on a set of eight samples at Laboratoire Magmas et Volcans (LMV, Clermont-Ferrand, France). Powdered samples were melted with $LiBO_2$ in a magnetic induction oven at 1100 °C for 5 min using graphite crucibles. The glass beads were then dissolved in a solution of deionized water and nitric acid (1 M) and diluted by a factor of 2000 to produce the solution analyzed by a HORIBA-Jobin-Yvon ULTIMA C ICP-AES. Analytical uncertainties (± 2σ) range between 1 and 3% except for Na_2O (7%) and P_2O_5 (10%). Three other samples (MAY181214-02, MAY181215-14a, and MAY181215-14b) were analyzed by "Plateforme Rayons X"-Université de Paris, with an X-ray fluorimeter Epsilon 3xl (Malvern-Panalytical) equipped with an Ag X-ray tube operating under He atmosphere, with 4 conditions during 120s: 5 kV– 60 µA without filter for the analysis of Na, Mg, Al and Si, 10 kV – 30 µA with a 7 µm titanium filter for the analysis of P, 12 kV – 25 µA with a 50 µm aluminium filter for the analysis of Ca, K and Ti, and 20 kV – 15 µA with a 200 µm aluminium filter during 120 s for the analysis of Mn and Fe. In order to avoid matrix and grain size effects, all samples were melted into "beads" prepared by mixing 0.1136 g of sample, 1.2312 g of fluxing agent ($LiBO_2/Li_2B_4O_7$) and 0.0187 g of non-wetting agent (LiBr) in a platinum crucible. The mixture was heated to 1050 °C for 25 minutes in a fusion instrument (LeNeo fluxer, Claisse). Calibration curves were obtained from identical beads of 14 geological reference materials (ACE, ANG, BCR-2, BEN, BHVO-2, BIR-1, BXN, DTN, FKN, GSN, MAN, Mica-Fe, Osh BO, UBN and BR24). The curves are perfectly linear over the entire concentration range. Analytical uncertainties (±1σ) are <5% for TiO_2, MnO and Fe_2O_3, 5% for MgO, SiO_2 and CaO, 10% for Al_2O_3, P_2O_5 and K_2O and 20% for Na_2O.

Trace elements analyses were performed by ICP-MS at Institut de physique du globe de Paris (IPGP, Paris, France). Around 50 mg of powdered rock samples were digested using a mix of 2 ml concentrated HNO_3 and 1 ml concentrated HF, heated in closed Teflon vessels at 110°C for 24 h. An additional 3 ml of concentrated HNO_3 was added to the samples after cooling and the mix was heated for another 24 h at 110 °C. Finally, 45 ml of ultrapure water was added to the samples after cooling and the solutions were sonicated for 4 hours. Samples were analyzed 24 to 48 hours later, after an additional 10x dilution with ultrapure water, using an inert introduction system on an Agilent 7900 ICP-MS. Calibration of rock samples was done against a BEN rock standard (Jochum et al. 2016). Analytical uncertainties are 6% or less for lithophile elements and 15% or less for chalcophile elements.

1.3. Electron microprobe analyses

Composition of minerals and glasses were analyzed using the CAMECA SXFive Tactis electron microprobe at LMV. We used an accelerating potential of 15 kV and a probe current of 15 nA (8 nA for glasses) for major and minor elements, with 10 s counting times. The beam was focused for minerals and defocused to a 20 µm diameter for glasses to avoid Na migration under the electron beam. Natural and synthetic mineral standards, including orthoclase (K, Al), albite (Na), wollastonite (Si, Ca), fayalite (Fe), forsterite (Mg), $TiMnO_3$ (Ti, Mn), NiO (Ni), Cr_2O_3 (Cr), and fluorapatite (P) were used for routine calibration.

4. Results

4.1. Whole-rock geochemistry

Major elements

Major element compositions of our collected samples are presented in Supplementary Tab. 1. Lavas from Mayotte volcanic ridge belong to the moderately silica-undersaturated trend identified for the Comoros magmas on Mayotte Island and at Karthala volcano on Grande Comore Island (Bachèlery et al. 2016; Pelleter et al. 2014). The distribution of lava compositions is bimodal, with basanites sampled both in the distal (active eruptive site, Berthod et al. 2021) and proximal part of the ridge (MAY02-DR06, MAY04-DR09), and phonolites sampled in three dredges on the proximal part of the ridge (MAY01-DR02, MAY02-DR06, MAY02-DR07). Mafic seamounts, with a SiO_2 content of 43.6 – 46.6 wt% and Na_2O+K_2O = 6.2 – 7.9 wt%, plot in the basanite/tephrite field of the TAS diagram (Fig. 2a), and according

to their normative olivine content should be classified as basanites. Their low MgO contents, between 4.5 and 6.4 wt%, and high FeO contents, 10.8 and 13.7 wt%, make them evolved basanites (Fig. 2b). Basanitic samples from the two dredges (MAY04-DR09 and MAY02-DR06) scattered along the ridge are very similar to lavas emitted at the 2018-2021 eruption site (Berthod et al. 2021, Fig. 2a). As already observed for the eruptive site (Berthod et al. 2021), evolved basanites of the volcanic ridge are characterized by an enrichment in P_2O_5 (0.9 – 2.0 wt%) compared to subaerial lavas from the Comoros archipelago (Supplementary Tab. 1). The basanitic sample collected on Petite Terre (MAY181214-02) displays more primitive compositions than MAY04-DR09 and MAY02-DR06 sample with SiO_2, Na_2O+K_2O, and MgO contents of 41.9 wt%, 2.9 wt%, and 15.4 wt%, respectively. The high CaO content however suggests that it is not a primitive mantle melt but contains accumulated clinopyroxenes.

Conversely, lava flows sampled in the proximal ridge area (MAY01-DR02, MAY02-DR07) and north of this site (MAY02-DR06, Fig. 1b) fall within the phonolite field of the TAS diagram with SiO_2 contents ranging from 56.1 to 57.5 wt% and Na_2O+K_2O contents of 12.6 – 13.0 wt% (Fig. 2a). Their low MgO and FeO contents (0.4 – 0.6 % and 6.2 – 6.5 %, respectively) reflect their differentiated character (Fig. 2b). The sample collected on Petite Terre (MAY181215-14b) also plots in the phonolite field with SiO_2, Na_2O+K_2O and MgO contents of 57.8 wt%, 5.6 wt%, and 1.2 wt%, respectively.

Only the largest mantle xenolith (MAY181215-14a) has been analyzed for bulk chemistry and is characterized by a high MgO content of 46.7 wt% and a low alkali content of 0.36 wt%.

Trace elements

The chondrite-normalized rare earth element (REE) patterns of the basanitic and phonolitic samples are distinct (Fig. 3a) with different concentrations, but both show a strong enrichment in light REE (LREE) compared to heavy REE (HREE). However, we note that phonolites are more fractioned in LREE while basanites are more fractioned in HREE. LREE/HREE ratios are lower in phonolites ($(La/Yb)_N$ = 17.5 – 23.0) than in basanites ($(La/Yb)_N$ = 21.93 – 27.87). The phonolite REE patterns crosscut those of the basanites in the middle to heavy REE range. In addition, contrary to the basanites, phonolites are characterized by negative europium anomalies.

Basanites and phonolites display different spider diagrams of incompatible trace elements normalized to chrondrite concentrations (Fig. 3b). In particular, phonolites are characterized by depletions of TiO_2, Sr, and, for some of them, Ba, compared to basanites.

Phonolites are more enriched in incompatible elements than basanites (Fig. 3c). Indeed, Th content vary from 5 to 9 ppm in basanite and from 15 to 24 ppm in phonolite. With Co content of 24 – 50 ppm in basanite and of < 1 ppm in phonolite, all samples are characterized by a well-defined trend of decreasing Co with decreasing MgO content (Fig. 3d). This is true for all other compatible elements (Cr, Ni…). Scandium contents, ranging from 12 to 16 ppm, do not vary between basanites and phonolites (Fig. 3e). Barium content decrease from 1833 to 329 ppm with increasing SiO_2 content (Fig. 3f).

Phonolite samples collected on Petite Terre display compositions close to submarine phonolites with Th, Co, Sc and Ba of 19 ppm,1 ppm, 15 ppm and 48 ppm, respectively (Fig. 3). The REE pattern is similar to submarine basanites except for the Eu anomaly which is more pronounced. The basanitic sample is characterized by similar Th and Co content (4 ppm and 60 ppm, respectively) and higher Sc contents (45 ppm) and a lower Ba content (200 ppm) compared to offshore basanites.

4.2. Petrology

The evolved basanites (MAY02-DR06 and MAY04-DR09) sampled at shallower water depth on the proximal part of the ridge and the mafic clast found scattered in the Moya phonolite maar (MAY181214-02) display a porphyritic texture with olivine and clinopyroxene crystals set in microcrystalline groundmasses (Fig. 4a-d). These evolved basanites contain numerous glomerocrysts of olivine and clinopyroxene, with frequent normal zoning. Some clinopyroxene crystals also show sector zoning (MAY02-DR06 samples). Olivine and clinopyroxene crystals are sometimes intergrown (Fig. 4c) indicating co-crystallization of these two phases. The groundmass consists of < 150 µm subhedral clinopyroxene microlites, which are occasionally zoned, and < 50 µm oxides. A few clinopyroxene glomerocrysts are characterized by three stages of growth including a rounded core surrounded by a rim with two stages of growth. The last stage is occasionally dendritic as observed in sample MAY02-DR060201m (Fig. 4d).

Dredged phonolites are characterized by a trachytic texture with < 200 µm iron-rich olivine (fayalite) microphenocrysts (Fig. 5). They have rounded (Fig. 5a) and/or skeletal (Fig. 5b) shapes and are intergrown with apatite and oxide crystals (Fig. 5c). The groundmass is composed of thin < 200 µm elongated alkali feldspars, < 100 µm apatite laths and < 50 µm euhedral oxide microlites (Fig. 5a, b, and c). There are two generation of feldspars in some

samples (Fig. 5b), with rare microphenocrysts and elongated microlites. One sample (MAY02-DR070207) contains a few large (> 5 mm) rounded alkali-feldspar crystals.

Glassy samples collected on land on Petite Terre show a similar trachytic texture and similar mineralogy. There, subhedral iron-rich olivine crystals are set in a groundmass containing < 50 μm feldspar microlites associated with small oxides (Fig. 5d).

Phonolitic samples (MAY02-DR07 offshore and MAY181215-14b on land) contain mantle xenoliths that range in size from a few mm (Fig. 6a, b) to more than 8 cm. Ultramafic xenoliths embedded in phonolites are mostly composed of large olivine and orthopyroxene crystals and small clinopyroxene and spinel crystals (Fig. 6b, c and d). The largest xenolith contains 73 % modal olivine, 23 % orthopyroxene, 2 % clinopyroxene and 2 % spinel as estimated by image analysis. Some of the orthopyroxene and clinopyroxene crystals contain exsolution lamellae (Fig. 6c and d). One of the xenoliths (MAY02-DR070208E) is crosscut by a vein containing phlogopite, pargasitic amphibole and a Ca-rich feldspar (Fig. 6b). The xenoliths are not in equilibrium with their host phonolite and are surrounded by a reaction rim (Fig. 6b). Reaction between olivine crystals and the phonolitic melt results in an overgrowth of new olivine enriched in iron, whereas reaction between orthopyroxenes and the phonolitic melt produces a thicker reaction-zone containing small olivine and oxide crystals.

4.3. **Phase compositions and equilibria**

Basanites

Basanites from dredge MAY02-DR06 are almost aphyric, and the small number of phenocrysts show evidence of disequilibrium. Olivine crystals are normally zoned, with a sharp transition between a rounded Mg-rich core ($Fo_{80.5 - 84.7}$) and a rim enriched in Fe ($Fo_{71.8 - 74.0}$, Fig. 7a, Supplementary Tab. 3). The rims are in equilibrium with the bulk rock composition ($Kd^{Fe-Mg}_{olivine-melt}$ = 0.32, compared to a theoretical value of 0.30, Roedder and Emslie 1970) whereas the cores are not ($Kd^{Fe-Mg}_{olivine-melt}$ = 0.15), pointing to a xenocrystic/antecrystic origin for the cores. Clinopyroxene phenocrysts are also characterized by rounded cores surrounded by a sieve-textured inner rim, and an outer rim with oscillatory zoning. MgO, Al_2O_3 and Cr_2O_3 variations in a zoned clinopyroxene are in favor of mixing with a more primitive melt (Fig. 4b). Magnesian cores (Mg# 70.6 – 81.9) are generally enriched in Al (up to 8.8 wt% Al_2O_3) and Na (up to 1.66 wt% Na_2O). Equilibrium is harder to assess for clinopyroxene compared to olivine,

but apart from three outlying analyses, most clinopyroxene cores could be in chemical equilibrium with the bulk rock composition ($Kd_{cpx-melt}^{Fe-Mg}$ = 0.28 ± 0.08, according to Putirka 2008). Rims (Mg# 66.9 – 76.4) have lower concentrations of Al (3.3 – 7.8% Al_2O_3) and Na (0.4 – 0.8 % Na_2O). In one crystal, the Mg# 73 core contains inclusions of an aluminous spinel (spinel-hercynite solid solution) and amphibole (hastingsite). Oxide crystals are titanomagnetites with 62.8 – 69.3 % FeO and 12.6 – 19.3 % TiO_2 (Fig. 7c, Supplementary Tab. 6).

Similarly to MAY02-DR06, olivine crystals in MAY04-DR09 samples are normally zoned, with a progressive compositional variation from $Fo_{85.3}$ to $Fo_{78.7}$ (Fig. 7a). The most primitive cores (Fo > 82 %) indicate that olivine cores are not in equilibrium with the bulk rock ($Kd_{olivine-melt}^{Fe-Mg}$ down to 0.12), pointing to partial accumulation of olivine and clinopyroxene, as suggested by the presence of glomerocrysts. Clinopyroxene crystals are also normally zoned, but with more discrete variations than olivine compositions and some amount of oscillatory zoning, and Mg# variations from 85.5 down to values as low as 59.4 (Fig. 7b). A few crystals contain rounded cores corresponding to the most magnesian compositions. Also, most of the crystals are characterized by sector zoning. As for olivines, clinopyroxene are not in chemical equilibrium with the bulk rock composition ($Kd_{cpx-melt}^{Fe-Mg}$ down to 0.14). As described by Ubide et al. (2019), Neave et al. (2019) and Haddadi (2016), the hourglass sectors are depleted in minor elements (Ti, Al, Mn, Na, and in our case also Fe), and comparatively enriched in Mg compared to the prism sectors. Oxide crystals are titanomagnetites with 47.5 – 68.5 % FeO and 6 – 15.6% TiO_2 (Fig. 7c). A few chromium-rich spinels with Cr_2O_3 ranging from 12.5 to 21.8% also occur as inclusion in some clinopyroxene crystals.

The primitive basanite sample from Petite Terre, MAY181214-02, is significantly enriched in large clinopyroxene and olivine crystals. Olivine crystals present a restricted compositional range ($Fo_{77.7 – 86.6}$, Fig. 7b). Contrary to samples MAY02-DR06 and MAY04-DR09, olivine cores could be close to equilibrium with the bulk rock ($Kd_{olivine-melt}^{Fe-Mg}$ = 0.27 – 0.28). Clinopyroxene crystals in this sample are similar to those in MAY02-DR06 and MAY04-DR09 samples, with large variations of Mg# (from 41.8 to 87.9, Fig. 7b) and Al_2O_3 (2.7 – 12.2 wt%). Most clinopyroxene crystals are normally zoned, with a rather abrupt and partially rounded transition between Mg# ~85 cores and more Fe-rich rims (Mg#69-78), suggesting a significant change in crystallization conditions. As for olivines, the most magnesian cores are in chemical equilibrium with the bulk rock composition ($Kd_{cpx-melt}^{Fe-Mg}$ = 0.26 – 0.35). One

normally zoned crystal containing large apatite inclusions is less magnesium-rich, with a Mg# between 71 and 65. According to mineral equilibrium this sample might be representative of a true liquid despite the abundance of large crystals (~ 40 % modal). However, elevated bulk CaO (15.45 wt%, Fig. 2c) and Sc (45.5 ppm, Fig. 3e) indicate at least some clinopyroxene accumulation.

Phonolites

Olivine crystals in submarine and subaerial phonolites are fayalites ($Fo_{17.6-31.6}$ and $Fo_{2.0-4.1}$ respectively) with 2.3 – 3.4 and 5.1 – 5.6 wt% MnO (Fig. 7a). They are intergrown with titanomagnetite (up to 18 wt% TiO_2) and apatite. Titanomagnetite crystals contain 72.1 – 78.4 wt% FeO, 10.4 – 18.3 wt% TiO_2, and 2.3 – 3.4 wt% Al_2O_3 (Fig. 7c). Alkali feldspar microlites are mostly anorthoclase ($Ab_{57.9-68.4}Or_{10.1-35.5}An_{6.2-23.8}$, Fig. 7d, Supplementary Tab. 5). The megacrysts are sodic sanidine ($Ab_{54.8}An_{42.1}Or_{3.2}$) with a rounded edge, separated by a sharp boundary from an anorthoclase overgrowth whose composition is intermediate between the composition of the megacrysts and that of the microlites. These megacrysts may be xenocrysts crystallized from a more differentiated magma or high-pressure antecrysts that became unstable during ascent.

Compositions of the glasses in most samples display a trend approximating a liquid line of descent (Fig. 2). The silica content in dredged phonolites glasses (MAY02-DR06, MAY01-DR02 and MAY02-DR07 dredges) varies from 56.8 to 60.5 % and MgO from 0.19 to 0.41 %. As SiO_2 increases, alkalis ($Na_2O + K_2O$) increase from 8.7 to 14.1 % and FeO content decreases from 6.4 to 4.4 wt%, respectively. Glasses from phonolites collected on Petite Terre Island present similar but more clustered compositions with SiO_2, MgO, alkalis and FeO contents of 57.6 – 60.1 %, 0.01 – 0.08 %, 14.4 – 15.1 %, and 4.5 – 4.8 %, respectively.

Xenoliths

Ultramafic xenoliths in phonolite lavas and pyroclasts are mantle fragments (harzburgite) dominated by Mg-rich olivine and orthopyroxene, with minor clinopyroxene and spinel. Olivine crystals are mantle olivine ($Fo_{90.2-93.1}$) which contain very little MnO (0.03 – 0.22 wt%) and low CaO concentrations (0 – 0.15 wt%). Pyroxenes are $Mg\#_{91.3-94.9}$ clinopyroxene and $Mg\#_{88.6-95.1}$ orthopyroxene with CaO contents of 17.1 – 24.8 % and 0.37 – 2.53 wt%, respectively. Oxides are chrome-spinel with Cr_2O_3 higher than 31% and FeO content ranging from 17.0 to 24.3 wt%. In one xenolith sample (MAY02-DR070208E), a vein contains a few crystals of bytownite plagioclase ($An_{76.7-88.2}$), pargasitic amphibole (Mg# 92) and

phlogopite mica (Mg# 91.2 – 93.2). Relationship between the three phases is difficult to assess, however, textural evidence indicates that at least some of the phlogopite grew as a reaction product between plagioclase and orthopyroxene. Phlogopite and amphibole are further destabilized along their edges to fine-grained mineral intergrowths. The highly magnesian nature of this mineral assemblage indicates it is fully equilibrated with the peridotite, and do not result from late reaction between the ascending phonolite magma and the xenolith. Where the vein is in contact with the host phonolite, minerals are dissolved, and recrystallization of more iron-rich micas (Mg# 51.2) is observed. This vein was thus formed through a previous step of melt percolation.

5. Discussion

Both phonolites and basanites are present on the proximal part of the volcanic ridge and onshore, on Petite Terre Island. Phonolites and basanites collected offshore and on land display similar textural, petrological and geochemical features (Figs 2 – 7). Proximal basanites have a porphyritic texture with a microcrystalline groundmass made of clinopyroxene microlites and Fe-Ti oxides (Fig. 4a, b, and c), and glomerocrysts of zoned olivine and sector-zoned clinopyroxene. By contrast, the eastern part of the submarine ridge is only built from basanites characterized by an aphyric texture (ongoing eruptive site, Berthod et al. 2021).

All these samples belong to a moderately silica-undersaturated alkaline series (Fig. 2) which corresponds to the Karthala trend (Bachèlery and Hémond, 2016). Also, geographically, all samples belong to a N140 alignment of numerous volcanic features (Fig. 1b, Feuillet et al. 2021). This 60 km long volcanic ridge runs on the eastern flank of Mayotte, from the site of a large active 2018-ongoing submarine eruption to the east, to Petite Terre Island to the west (Fig. 1b). The existence of this ridge raises two main scientific questions: (1) What is the origin of the phonolites, and are they related to the basanites? (2) Is the entire volcanic ridge, on land and offshore, fed by the same plumbing system or are there numerous ascent pathways and magma storage zones? To answer these questions, it is necessary to understand how this compositional bimodality is achieved.

Since the phonolites contain mantle xenoliths (Fig. 6), they were generated below the Moho, i.e., deeper than 17 km (Dofal et al. 2018). Most phonolites are generated by fractional crystallization in shallow crustal magma chambers (< 10 km, Grant et al. 2013 and references therein), and evidence for phonolitic melts at mantle depth is scarce (e.g., Price and Green 1972; Dautria et al. 1983; Grant et al. 2013). It has been demonstrated that phonolites can be directly

produced by mantle melting (Irving and Price, 1981; Laporte et al. 2014; Loges et al. 2019). Such phonolites have low FeO concentrations (2 – 3 wt%) and are in equilibrium with high Mg# olivines (~Fo_{90}, Laporte et al. 2014). Phonolitic glasses in equilibrium with mantle compositions have been analyzed in lherzolitic mantle xenoliths from La Grille on Grande Comore (Coltorti et al. 1999), and indeed show high Mg# (59 – 78) and low FeO concentrations (<3.1 wt%). The investigated phonolites of the Mayotte ridge, however, are highly evolved, with a significant enrichment in FeO (6.1 – 6 5 wt%) and are in equilibrium with low Mg# olivines (Fo_{13-28}), precluding an origin by direct mantle melting. The differentiated character of those phonolites would thus be better explained by fractional crystallization of a more primitive magma in a mantle reservoir.

5.1. Evidence of fractional crystallization

No primitive composition in equilibrium with a mantle lherzolite has been erupted along the ridge. This indicates the presence of one or more reservoirs in which the magma evolves between the source and the surface. According to our previous studies (Berthod et al. 2021; Feuillet et al. 2021), there are at least two levels of magma storage, one near 40 - 50 km depth in which the primitive magma differentiated to form the evolved basanites, and one upper level, possibly between 15 and 20 km, where some more evolved magma is stored.

The evolution of igneous suites by fractional crystallization is characterized by decreasing concentration of compatible trace elements whereas incompatible elements increase and have near-constant ratios with each other (Kyle et al. 1992). According to our major and trace element data, the fractionating assemblage likely includes clinopyroxene (decrease in CaO and Sc, Fig. 2c and 3e), feldspar (negative Eu anomaly, decrease in Ba and Sr, Fig. 3), magnetite and ilmenite (decrease in FeO, TiO_2, and Co, Figs 2 and 3), apatite (strong decrease in P, Supplementary Tab. 1) and possibly olivine (decrease in MgO, Ni and Co, Figs 2 and 3). There is no evidence for the crystallization of hydrous minerals (amphibole, mica), which usually produce negative anomalies in K_2O, Rb, and high field strength elements like Nb, Ta, Zr and Hf (Matsui et al. 1977; Schnetzler and Philpotts, 1970).

The volcanism of the ridge extending from Petite Terre to the 2018 - 2021 eruption site is strongly bimodal, and no intermediate compositions between evolved basanites and phonolites have been sampled so far despite three dredging campaigns and two sampling missions on land. This compositional gap commonly observed in tholeiitic and calc-alkaline series (e.g., Daly (1925), Grove and Donnelly-Nolan (1986), Reubi and Blundy (2009)) is rarely

observed in alkaline series. This feature complicates petrological modelling but does not in any way precludes an origin for the phonolites by differentiation of the basanites.

The possibility of a genetic link between basanites and phonolites was tested through a series of fractionation models: (1) Melts model, for major elements coupled with mass balance, and (2) trace element correlation model.

5.2. Fractional crystallization tested with MELTS models and mass balance

Fractional crystallization models were run using the Rhyolite-MELTS software (Ghiorso and Gualda, 2015; Ghiorso and Sack, 1995; Gualda et al. 2012). We used the bulk composition of evolved basanite MAY01-DR0101 collected at the 2018-2021 eruption site as parental melt (Berthod et al. 2021). For each model, temperature decreased from 1200 to 700 °C, with a 10 °C step. Since no orthopyroxene and garnet crystals were found in Comoros lavas, they were excluded from the crystallizing assemblage. We tested a range of possible pressures from 0.2 to 1.2 GPa, H_2O concentrations from 1.0 wt% to 5.0 wt% (up to 2.3 wt% H_2O as measured in olivine-hosted melt inclusions, Berthod et al. 2021), and a range of oxygen fugacities buffered between FMQ+1 and FMQ-2. Results of our Rhyolite-MELTS models are presented on Fig. 8. All models are characterized by early crystallization of clinopyroxene, apatite and magnetite starting above 1100 °C. A second crystallization stage involves anorthoclase and biotite with very late-stage leucite in some models. Early crystallization of olivine appears at low pressure and low oxygen fugacity. Ilmenite crystallizes in all models with $H_2O \leq 3.0$ % and generally appears early at high pressure and low oxygen fugacity. We observed that an increase in the initial H_2O concentration decreases the crystallization temperatures and the onset of feldspar crystallization relative to clinopyroxene/olivine/Fe-Ti-oxide but only have a limited impact on the crystallization path. An increase in pressure produces a strong increase in FeO and Na_2O concentrations in the residual melt (Fig. 8). This is correlated with the involvement of more clinopyroxene, particularly early on, a decrease in magnetite and ilmenite contents, and absence of olivine. Variations in oxygen fugacity have a similar impact to pressure, with lower oxygen fugacity decreasing the amount of clinopyroxene and magnetite and resulting in higher FeO and Na_2O contents. Therefore, the exceptional FeO content in Petite Terre and submarine ridge phonolites (Fig. 8) may be a consequence of a deeper fractionation level compared to most phonolites (Grant et al. 2013; Moussallam et al. 2013; Scaillet et al. 2008) and/or particularly low oxygen fugacity. This observation is supported by the fact that the best fits to the phonolite composition are obtained at higher

pressures and lower oxygen fugacities. The overall best model is obtained at 0.6 GPa with 2.3 wt% H_2O and an oxygen fugacity at FMQ-1 (Fig. 8), with a crystallizing assemblage of olivine (12.5 %), magnetite (15.5 %), apatite (5 %), ilmenite (4 %) and clinopyroxene (34 %) at high temperature, and anorthoclase (30%) below 1000 °C. The lower role of the clinopyroxene fractionation compared to the early fractionation stages (80 %, Berthod al. 2021) is supported by the scandium contents which do not vary between basanites and phonolites (Fig. 3e). Further crystallization after reaching the composition of MAY02-DR07 / MAY01-DR02 phonolites produces biotite, anorthoclase and leucite. Small amounts of fayalite crystallize in the lower oxygen fugacity models (FMQ-1 and lower). The presence of fayalite microlites in the phonolites is thus likely indicative of low oxygen fugacity, as confirmed by experimental studies (Giehl et al. 2013; Romano et al. 2020; Rutherford, 1969).

The phonolites from the ridge are characterized by an unusual enrichment in iron, compared to older phonolites from the main island of Mayotte (Debeuf, 2004; Pelleter et al. 2014, Fig. 8), and most phonolites worldwide. This iron enrichment, akin to the trend observed in the tholeiitic series (e.g. Carmichael 1964) has already been described in some lavas from the East African Rift (Barberi et al. 1971; Nash et al. 1969) and in the peralkaline rocks of the Gardar province in Greenland (Marks and Markl, 2003). Iron enrichment is usually explained by a late involvement of magnetite in the crystallization sequence (Chin et al. 2018; Luhr et al. 1984), possibly a consequence of low oxygen fugacity (e.g., Marks and Markl 2003, Nash et al. 1969) and/or low water content (Tatsumi and Suzuki, 2009). These observations are in agreement with the Rhyolite-MELTS model, which suggests reducing conditions, and magma storage and evolution at upper mantle levels.

To confirm the Rhyolite-MELTS model, we performed a simple least-squares mass balance using major elements (Bryan et al. 1969). The calculation starts from the same composition (MAY01-DR0105 sample, Berthod et al. 2021) and ends with the composition of MAY01-DR020202 phonolite. We use microprobe analyses of phenocrysts and microlites from MAY01-DR0105 (olivine, clinopyroxene, magnetite, apatite), MAY02-DR08 (ilmenite) and MAY01-DR02 (anorthoclase and fayalite). The best model implies the crystallization of anorthoclase (50%), olivine (18 %), clinopyroxene (15 %), magnetite (8 %), apatite (5 %), and ilmenite (4 %). We note that changes in the crystallizing mineral composition are not considered in this simple model, which likely explains the significant differences in modal proportions of

anorthoclase and clinopyroxene between the mass balance calculation and the chosen Rhyolite-MELTS crystallization model.

5.3. **Fractional crystallization tested with trace elements model**

Trace element compositions of basanites found along the submarine ridge are similar to those reported for the 2018 - 2021 ongoing eruption (Fig. 3b, Berthod et al. 2021), and for the entire Comoros archipelago (Bachèlery and Hémond, 2016; Class et al. 1998; Claude-Ivanaj et al. 1998; Deniel, 1998b; Späth et al. 1996).

REE are strongly fractionated ($(La/Yb)_N$ = 21.9 – 27.9), indicating a deep peridotitic source with residual garnet, in agreement with previous studies on subaerial Comoros lavas. This suggests that primary magmas are produced by small degrees of partial melting near the spinel / garnet boundary, i.e. 80 – 100 km, (Bachèlery and Hémond, 2016; Class et al. 1998; Claude-Ivanaj et al. 1998; Deniel, 1998b; Späth et al. 1996) and our previous study of the ongoing 2018-2021 eruption (Berthod et al. 2021).

Phonolite and basanite lavas display similar REE enrichment but with significantly different patterns (Fig. 3a and b). In fact, phonolite REE patterns are less fractionated ($(La/Yb)_N$ = 17.12 – 22.54) than the basanites ($(La/Yb)_N$ = 14.43 – 29.78), which could suggest a different shallower source within the spinel stability field (Fig. 8a). In addition, if phonolites are derived from basanites by fractional crystallization, REE contents should be more enriched than the mafic parental magma. To obtain similar patterns, the fractionated assemblage must include a REE-rich mineral that preferentially fractionates middle REEs. All basanitic samples are characterized by an excess of phosphorus, also observed in all glass analyses (Fig. 9a), suggesting that apatite crystallization might play a role. In fact, apatite-melt REE partition coefficients can reach high values (up to 21.7 for La, Luhr et al. 1984; Fujimaki 1986; Mahood and Stimac 1990; Prowatke and Klemme 2006). Using these high partition coefficients and an amount of fractionated apatite estimated from the glass phosphorus content, we can reproduce the phonolite REE pattern (Fig. 9b, and Supplementary Tab. 7). Therefore, we suggest that the difference in REE patterns between basanites and phonolites do not reflect a different source but are solely a consequence of apatite crystallization.

To confirm the major element models, phase proportions in the fractionated assemblage were independently estimated using the model proposed by Villemant et al. (1981) based on trace element variations in a monotonous fractionation series. In their model, bulk partition

coefficients are extracted from correlations between a given trace element and a perfectly incompatible reference element, usually Th. In Mayotte samples, a few elements (Nb, Ta, Zr, Cs) are more incompatible than Th, so we used Cs, the most incompatible element, instead of Th. This is usually not done because of the high mobility of Cs, however, given the very young age of the investigated rocks, there is a very good correlation between Cs and Th ($r^2 = 0.972$) indicating that Cs mobility was negligible. We then selected a series of trace elements for which (1) the correlation with Th and Cs is good ($r^2 > 0.90$) or the value is constant, and (2) there is a good set of mineral/melt partition coefficient available (partition coefficients taken from Adam and Green (2006), Stix and Gorton (1990), Klemme et al. (2006) and Mahood and Stimac (1990)). We then performed a multiple regression analysis following Villemant et al. (1981) to extract the proportions of minerals in the fractionated assemblage, from the bulk partition coefficients and individual mineral partition coefficient. We only use minerals that have been observed in at least one dredged sample, i.e., olivine, clinopyroxene, magnetite, ilmenite, anorthoclase, and apatite. There is no break in slope in the log/log correlation, suggesting that the fractionating assemblage is relatively constant, at least within the resolution of our model, which is limited by the absence of intermediate compositions in the phonotephrite/tephriphonolite fields. HFSE are among the most incompatible elements, equally or more incompatible than Th, which preclude the crystallization of amphiboles or micas. Phase proportions in the crystallizing assemblage, obtained with this trace element model, are dominated by feldspar (54 %), clinopyroxene (26 %), olivine (12 %), and apatite (8 %), with a negligible amount of magnetite. These results are in good agreement with the Rhyolite-MELTS model, and the mass-balance calculations.

5.4. Evidence of multiple levels of magma storage

Basanitic mantle reservoirs

As evidenced for lavas emitted by the 2018-2021 ongoing eruption on the eastern part of the submarine volcanic ridge (Fig. 1b), the low Mg# of the basanites indicates that they are not primary mantle melts (Berthod et al. 2021). This is supported by the presence of zoned olivine and clinopyroxene phenocrysts, which typically grow in dynamic reservoirs undergoing frequent replenishments and drainages (Fig. 4).

In addition, our barometric study of the clinopyroxene phenocrysts (Putirka, 2008) indicate multiple levels of magma storage beneath the volcanic ridge (Fig. 10, Supplementary Tab. 8). Since clinopyroxene compositions are neither in equilibrium with the bulk rocks nor in

equilibrium with the residual glasses, the Putirka (2008) clinopyroxene-only geobarometer (equation 32a) is the most accurate geobarometer, with a standard error of estimate of 0.28 GPa (9 km). Assuming an average density of 2,890 $kg.m^{-3}$ for the oceanic crust and 3,300 $kg.m^{-3}$ for the lithospheric mantle, we estimate that the cores of clinopyroxene phenocrysts ($Mg\#_{82-73}$) in MAY02-DR06 basanite sample crystallized during a first phase of growth in a basanitic magma reservoir located at about 37 – 50 km depth (Fig. 10). The location of this deep magma reservoir is in excellent agreement with seismicity location (ReVoSiMa, 2021) and is consistent with the previous geophysical studies (Cesca et al. 2020; Feuillet et al. 2021; Lemoine et al. 2020) and our previous geobarometric study on 2018-2021 erupted lavas which proposed a ≥ 37 km deep mantle reservoir (Berthod et al. 2021). However, few clinopyroxene crystal cores in the MAY02-DR06 basanite sample return a depth range of 57 – 63 km (Fig. 10). These depths do not overlap the deepest earthquake hypocentres (Fig. 11), even within the +/- 9 km uncertainty. Therefore, we propose that our barometric results highlight a second deeper reservoir located between 57 and 63 km depth (Figs 10 and 11). Oscillatory zoned outer rims clinopyroxene phenocrysts ($Mg\#_{67-73}$) in MAY02-DR06 basanite sample crystallized during a second phase of growth in a shallower more differentiated basanitic magma chamber at an average depth of 18 ± 9 km (0.47 ± 0.28 GPa, Fig. 10).

Similar results have been obtained for sector-zoned clinopyroxene glomerocrysts in the MAY04-DR09 basanite sample. A few deep resorbed clinopyroxene cores ($Mg\#_{83-8}$, Fig. 10) crystallized at a pressure of 1.19 ± 0.28 GPa equivalent to a depth of 40 ± 9 km. For the sector-zoned rims, we only used the Al_2O_3-rich prism sectors for barometry calculations, since hourglass sectors have been shown to produce erroneous pressure (Neave et al. 2015). Except for the resorbed cores, barometry indicates that clinopyroxene crystals ($Mg\#_{59-82.5}$) formed at intermediate pressures similar to those obtained for MAY02-DR06: 0.43 ± 0.28 GPa (16 ± 9 km, Fig. 10).

For the MAY181214-02 basanite sample collected on Petite Terre, no evidence was found for a deep fractionation level, and a mean depth of 17 ± 9 km (clinopyroxene $Mg\#_{47.9-67.5}$) has been calculated from phenocrysts and rims of the zoned clinopyroxene antecrysts (Fig. 10). Since MAY181214-02 ankaramite corresponds to an old lithic fragment collected on Petite Terre, our results suggest a stable depth for the shallower magmatic system feeding both on land and offshore part of the active volcanic ridge of Mayotte through time.

Our geobarometric results allow us to propose multiple mantle storage levels: two deep mantle storages located below 40 km (Figs 10 and 11) and another shallower storage at about 15 – 20 km, near the Moho (Moho depth estimated at ~17 km, Dofal et al. 2018). However, the

large range of clinopyroxene compositions and zoning patterns preclude an identical transfer path for each magma pulse.

Phonolitic mantle reservoir

Phonolitic lavas contain clinopyroxene-bearing harzburgite xenoliths (Fig. 6). These fragments of mantle peridotite, incorporated into the phonolitic magma as it rose to the surface, indicate that they ascended from the mantle. In order to estimate the minimum depth of the phonolitic reservoir(s), we used a geothermobarometer (Putirka, 2008) on a series of clinopyroxene-orthopyroxene pairs in the mantle xenoliths (Fig. 6, Supplementary Tab. 9). These geobarometric calculations also provide the minimum depth of the Moho below the investigated area. Temperatures were calculated using equation (36) of Putirka et al. (2008) with reported uncertainties of 45 °C (see Berthod et al. 2021 for discussion). For pressure, both equations (38) and (39) were tested against experiments performed at 1.00 GPa by Condamine and Médard (2014). Since equation (38) returned an average pressure of 1.02 GPa, whereas equation (39) returned a less accurate average pressure of 0.88 GPa, equation (38) was thus preferred for the calculation. It reproduces the experimental data with an average error (SEE) of 0.19 GPa. Calculations performed on clinopyroxene-orthopyroxene pairs in textural equilibrium and on exsolutions (Fig. 6) give identical results. Assuming an average density of 2,890 $kg.m^{-3}$ for the oceanic crust and 3,300 $kg.m^{-3}$ for the lithospheric mantle, mantle xenoliths from phonolitic pyroclastic deposits from Petite Terre were equilibrated at the following depths (Fig. 10): 11.9 ± 3.4 km (MAY181215-14a), 12.3 ± 3.7 km (MAY190911-6a), 18.3 ± 5.4 km (MAY190911-4a), 14.5 ± 0.4 km (MAY190911-4b), 12.4 ± 2.9 km (MAY190911-4c) and 14.5 ± 2.1 km (MAY190911-4d). Clinopyroxene-orthopyroxene pairs were also analyzed in two more mantle xenoliths from phonolites of the submarine ridge and give similar equilibration depths of 15.2 ± 2.3 km (MAY02-DR070207) and 11.0 ± 1.3 km (MAY02-DR070208-xen, Fig. 10).

These depths are consistent with seismic data locating the Moho at about 17 km (Dofal et al. 2018), with the existence of numerous very low frequency seismic events between 10 and 30 km depths (Laurent et al. 2019, Feuillet et al. 2021), and with magnetotelluric sounding performed on the volcanic region (Darnet et al. 2020) which suggests the presence of magmatic conductive fluids at depth > 15 km. This is also coherent with the presence of an evolved magma batch located above 17 ± 6 km (0.45 ± 0.19 GPa) intersected by the June 2019 lava flow at the active volcanic site (sample MAY02-DR08, Berthod et al. 2021). Finally, results from the

672 Rhyolite-MELTS model confirm that differentiation occurred at about 20 km depth (0.6 GPa,
673 Fig. 8).
674 Similar minimum storage depths have been obtained for phonolites sampled on Petite
675 Terre and on the intermediate part of the volcanic ridge. This raises the question as to whether
676 these depths correspond to a single magma reservoir or to a zone made of several magma lenses.
677 We suggest that the hundreds seamounts constituting the 60 km-long and 31 km-wide volcanic
678 ridge (Fig. 1b) were probably emplaced between the last volcanic activity at Petite Terre (i.e.
679 about 4000 years ago, Zinke et al. 2003) and the currently ongoing eruption. As shown by
680 Castruccio et al. (2017), monogenetic volcanic fields are likely to be fed by ephemerous
681 superficial magmas lenses rather than long-lived reservoirs.
682 We note that the evidence of multiple magma storage reservoirs can also explain the
683 bimodal volcanism. However, the minimum depth of the phonolitic storage obtained from the
684 xenoliths is similar to the shallower basanitic reservoir (Fig. 10) located at about 15 – 20 km
685 depth. Therefore, we can evaluate the possibility that phonolites are products of differentiation
686 of basanite magmas in the shallower reservoirs located close to the Moho seismic discontinuity
687 interpreted as the mantle-crust interface.
688
689 **5.5. Integration in the geological context of Mayotte: possible eruption triggers?**
690
691 Berthod et al. (2021) demonstrated that 50 % crystallization of a cumulate containing
692 80 % clinopyroxene and 20 % olivine is required to generate the basanite from a primary mantle
693 melt in the deeper mantle reservoir (below 37 km, Fig. 11). Our barometric results on the
694 MAY02-DR06 sample demonstrated that the primary magma could come from an even deeper
695 reservoir located between 57 and 63 km depth (Figs 10 and 11). We then propose three
696 scenarios for magma evolution beneath the volcanic ridge: (1) the basanitic magma rises
697 directly and rapidly to the surface from the deep magma reservoir as evidenced by the
698 petrological characteristics of the ongoing eruption (Berthod et al. 2021) and seismological data
699 (Cesca et al. 2020; Feuillet et al. 2021; Lemoine et al. 2020); (2) zoned clinopyroxene
700 phenocrysts in some basanitic lavas at proximal seamounts MAY02-DR06 and MAY04-DR09
701 and on Petite Terre indicate that the basanitic magma stalls briefly at the Moho interface before
702 resuming its ascent toward the surface; (3) the basanitic magma stops and evolves to phonolite
703 in a reservoir below the Moho. In this third scenario, the phonolitic magma might be reactivated
704 by the arrival of a deeper and more primitive magma sourced from a deep reservoir > 30 km.
705 In that scenario, the absence of phenocrysts in the phonolites could be explained by an increase

706 in temperature induced by the self-mixing reactivation (Couch et al. 2001), although an
707 extremely efficient extraction process, or dissolution during ascent as a consequence of a
708 steeper liquidus slope compared to the adiabat cannot be excluded at this stage.
709
710 Our three different models show that the phonolitic lavas can be produced by
711 approximately 80 % fractional crystallization of a hydrous basanitic magma at mantle depths
712 (P > 0.6 GPa) under reduced oxygen fugacity (~FMQ-1). The total volume of MAY02-DR07
713 lava flow is estimated at 0.45 km^3, therefore, the volume of basanite necessary to generate this
714 phonolitic lava flow is at least 1.6 km^3. Taking into account the 50 % crystallization in the
715 deeper mantle reservoir, the eruption of 0.46 km^3 of phonolitic magmas thus requires intrusion
716 of 4.6 km^3 of primary mantle melts.
717
718 Since 2018, Mayotte is the site of unprecedented and unexpected volcanic and seismic
719 activities (Feuillet et al. 2021; Cesca et al. 2020; Lemoine et al. 2020). Following an
720 oceanographic campaign, Feuillet et al. (2021) demonstrated that the hundreds of seismic
721 events were associated with the development of a large volcanic edifice. As of January 2021,
722 the volcano has risen 820 m above the 3,300 m deep seafloor with an erupted lava volume of ~
723 6.5 km^3 (Feuillet 2019; ReVoSiMa 2021) which represents by far the largest observed
724 submarine eruption (Clague et al. 2011; Resing et al. 2011; Caress et al. 2012; Chadwick et al.
725 2016; Carey et al. 2018; Chadwick Jr et al. 2018) and the third largest mafic eruption of the last
726 two millennia (Thordarson and Self 1993; Thordarson et al. 2001; Oppenheimer et al. 2018;
727 Patrick et al. 2020). Berthod et al. (2021) demonstrated that this ongoing eruption is fed by a
728 deep (≥ 37 km) and large (≥ 10 km^3) mantle reservoir of evolved, alkaline magma having
729 experienced extensive crystallization (50 %).
730 This volcanic edifice is located on a N140 volcanic ridge that runs off the eastern flank of
731 Mayotte and whose subaerial expression is Petite Terre Island (Feuillet et al. 2021, Fig. 1b), a
732 ridge composed of hundreds of volcanic edifices (Fig. 1b). Large phonolitic lava flows are
733 present on this ridge, about 10 – 15 km East of Petite Terre (Fig. 1b). Pyroclastic phonolitic
734 edifices are also present on the submarine ridge and on Petite Terre. If phonolites derive by
735 fractional crystallization from basanitic lavas similar to those feeding the ongoing eruption, and
736 the structure of the plumbing system is similar all along the ridge, we suggest that the entire
737 volcanic ridge could be fed by the same magmatic system. Moreover, geological mapping of
738 the more than 300 submarine cones and vents clearly show that the zone of the Horseshoe 5 –
739 15 km from Petite Terre is the area with the highest density of individual eruptive vents per km^2

740 of the entire ridge (Fig. 1b). The extensive diversity of eruptive vents, eruptive styles, both
741 explosive and effusive, the magma bimodal composition, the large erupted volumes and
742 multiple superimposed eruptive cones and lava domes suggests that volcanism in the Horseshoe
743 area has been fed by a long-lasting and extensive transcrustal magmatic system that forms the
744 core of the magmatic system branching out to the West towards the Petite Terre recent Holocene
745 volcanic centers as well as branching out to the East towards the rest of the chain. The results
746 of our petrological analysis coupled with seismic data (Cesca et al. 2020; Lemoine et al. 2020;
747 Feuillet et al. 2021) support the hypothesis that this transcrustal magmatic system is currently
748 undergoing a massive reactivation that is feeding the current exceptional voluminous submarine
749 eruption. In such a model, existing phonolitic magma lenses could be reactivated by reinjection
750 of the basanitic magma feeding the ongoing eruption (Sparks et al. 1977). Although no evidence
751 of mingling or mixing has been identified in the phonolites so far, the presence of reversed
752 zoned olivine phenocrysts in the recently erupted basanite lavas (Berthod et al. 2021) suggest
753 that mixing involving a small shallow differentiated magma reservoir located close to the Moho
754 ($< 17 \pm 6$ km) did occur beneath the current eruption site. This indicates that if eruptible magma
755 is still present in lenses of the transcrustal mush magmatic system located at Moho depth
756 underneath the ridge, it could be reactivated by the arrival of a deeper and more primitive
757 magma. Such a scenario would have major implications in terms of increased volcanic hazard
758 for Mayotte on land. More than 300,000 people are living on Mayotte with about 70,000 in the
759 capital Mamoudzou located within the Holocene phreatomagmatic explosive volcanic zone,
760 and 30,000 people on Petite Terre Island which hosts the only international airport of the
761 archipelago, the electric plant and other economical and industrial assets as well as most of the
762 public administration.
763
764 ## 6. **Conclusion**
765 Our petrological study shows that the hundreds of edifices, individual cones and lava flows
766 forming the active volcanic ridge on the east flank of Mayotte Island are characterized by a
767 bimodal chemical distribution of erupted magmas, with basanite and phonolite but no
768 intermediate compositions. Trace element characteristics indicate that those lavas result from
769 partial melting near the garnet – spinel transition zone, between 80 – 100 km, which is
770 consistent with the structure of the of lithosphere in the region. Basanitic magmas are first stored
771 and evolve in deep magma reservoirs located between 35 and 60 km. Clinopyroxene barometry
772 highlights the existence of a second shallower storage system at about 15 – 20 km, probably
773 made of multiple lenses of basanitic and phonolitic magmas that form an extensive and long-

774 lasting transcrustal mush magmatic system. Basanitic magmas evolve to phonolites by about
775 81 % fractional crystallization in this shallow storage system.
776 Three scenarios are proposed: (1) the basanitic magma can rise directly and quickly to the
777 surface from the deep magma reservoir (current ongoing activity, Berthod et al. 2021). (2) the
778 basanitic magma stalls in a shallower reservoir near the Moho before resuming its ascent toward
779 the surface. (3) the basanitic magma stops and evolves to phonolite in the shallower magma
780 storage zone. In this third scenario, the phonolitic magma might be reactivated by the arrival of
781 a new batch of deeper basanitic magma. If the entire volcanic ridge is fed by the same extensive
782 plumbing system sourcing the transcrustal mush magmatic system below the Horseshoe area,
783 5 – 15 km East of Petite Terre, the current reinjection of basanitic magma feeding the ongoing
784 voluminous eruption could reactivate the phonolitic reservoirs that fed the volcanic areas on
785 Petite Terre and the volcanic ridge crossing the eastern flank of Mayotte, drastically increasing
786 volcanic hazards for the island of Mayotte. This is of particular concern given that Berthod et
787 al. (2021) have shown that the timescales that separated the last geochemical perturbation of
788 eruptible magma in a shallow Moho-depth storage zone recorded by zoned crystals, and the
789 arrival of the magma on the surface were on the range of 30 ± 4 days.
790

791 **Acknowledgements**

792 MAYOBS 1 campaign was funded by the CNRS-INSU TELLUS MAYOTTE program
793 (SISMAYOTTE project). MAYOBS 1, 2 and 4 campaigns were conducted by several French
794 research institutions and laboratories (IPGP/CNRS/BRGM/IFREMER/IPGS). We want to
795 thank the crew of R/V Marion Dufresne (TAAF/IFREMER/LDA). Analyses were funded by
796 the Service National d'Observation en Volcanologie (SNOV, INSU) and the Réseau de
797 Surveillance Volcanologique et Sismologique de Mayotte (REVOSIMA), a partnership
798 between the Institut de Physique du Globe de Paris (IPGP), the Bureau de Recherches
799 Géologiques et Minières (BRGM), and the Observatoire Volcanologique du Piton de la
800 Fournaise (OVPF-IPGP), the Centre National de la Recherche Scientifique (CNRS), and the
801 Institut Français de Recherche pour l'Exploitation de la Mer (IFREMER). The authors would
802 like to thank IFREMER for their welcome during the sampling and E. Humler for his support
803 and national funding coordination (CNRS, REVOSIMA). Finally, we are also grateful for the
804 helpful reviews provided by Peter Ulmer and an anonymous reviewer. This is a Labex ClerVolc
805 contribution number XXX.
806

807 **References**

808 Ablay, G.J., Carroll, M.R., Palmer, M.R., Martí, J., Sparks, R.S.J., 1998. Basanite–phonolite
809 lineages of the Teide–Pico Viejo volcanic complex, Tenerife, Canary Islands. J. Petrol.
810 39, 905–936. https://doi.org/10.1093/petroj/39.5.905
811 Adam, J., Green, T., 2006. Trace element partitioning between mica-and amphibole-bearing
812 garnet lherzolite and hydrous basanitic melt: 1. Experimental results and the
813 investigation of controls on partitioning behaviour. Contrib. to Mineral. Petrol. 152, 1–
814 17. https://doi.org/0.1007/s00410-006-0085-4
815 Bachèlery, P., Hémond, C., 2016. Geochemical and Petrological Aspects of Karthala
816 Volcano, in: Active Volcanoes of the Southwest Indian Ocean. Springer, pp. 367–384.
817 Bachèlery, P., Morin, J., Villeneuve, N., Soulé, H., Nassor, H., Ali, A.R., 2016. Structure and
818 eruptive history of Karthala volcano, in: Active Volcanoes of the Southwest Indian
819 Ocean. Springer, pp. 345–366.
820 Barberi, F., Bizouard, H., Varet, J., 1971. Nature of the clinopyroxene and iron enrichment in
821 alkalic and transitional basaltic magmas. Contrib. to Mineral. Petrol. 33, 93–107.
822 Berthod, C., Médard, E., Bachèlery, P., Gurioli, L., Di Muro, A., Peltier, A., Komorowski, J.,
823 Benbakkar, M., Devidal, J., Langlade, J.., Besson, P., Boudon, G., Rose-Koga, E.,
824 Deplus, C., Le Friant, A., Bickert, M., Nowak, S., Thinon, I., Burckel, P., Hidalgo, S.,
825 Jorry, S., Fouquet, Y., Feuillet, N., 2021. The 2018-ongoing Mayotte submarine
826 eruption: magma migration imaged by petrological monitoring. Earth Planet. Sci. Lett.
827 571, 117085, https://doi.org/10.1016/j.epsl.2021.117085
828 Bertil, D., Regnoult, J.M., 1998. Seismotectonics of Madagascar. Tectonophysics 294, 57–74.
829 https://doi.org/10.1016/S0040-1951(98)00088-2
830 Castruccio, A., Diez, M., Gho, R., 2017. The influence of plumbing system structure on
831 volcano dimensions and topography. J. Geophys. Res. Solid Earth 122, 8839–8859.
832 https://doi.org/10.1002/2017JB014855
833 Cesca, S., Letort, J., Razafindrakoto, H.N.T., Heimann, S., Rivalta, E., Isken, M.P., Nikkhoo,
834 M., Passarelli, L., Petersen, G.M., Cotton, F., Dahm, T., 2020. Drainage of a deep
835 magma reservoir near Mayotte inferred from seismicity and deformation. Nat. Geosci.
836 13, 87–93. https://doi.org/10.1038/s41561-019-0505-5
837 Chin, E.J., Shimizu, K., Bybee, G.M., Erdman, M.E., 2018. On the development of the calc-
838 alkaline and tholeiitic magma series: A deep crustal cumulate perspective. Earth Planet.
839 Sci. Lett. 482, 277–287. https://doi.org/10.1016/j.epsl.2017.11.016
840 Class, C., Goldstein, S.L., 1997. Plume-lithosphere interactions in the ocean basins:

841 constraints from the source mineralogy. Earth Planet. Sci. Lett. 150, 245–260.
842 Class, C., Goldstein, S.L., Altherr, R., Bachèlery, P., 1998. The process of plume–lithosphere
843 interactions in the ocean basins—the case of Grande Comore. J. Petrol. 39, 881–903.
844 https://doi.org/doi.org/10.1093/petroj/39.5.881
845 Class, C., Goldstein, S.L., Shirey, S.B., 2009. Osmium isotopes in Grande Comore lavas: a
846 new extreme among a spectrum of EM-type mantle endmembers. Earth Planet. Sci. Lett.
847 284, 219–227. https://doi.org/10.1016/j.epsl.2009.04.031
848 Class, C., Goldstein, S.L., Stute, M., Kurz, M.D., Schlosser, P., 2005. Grand Comore Island:
849 A well-constrained “low 3He/4He” mantle plume. Earth Planet. Sci. Lett. 233, 391–409.
850 https://doi.org/10.1016/j.epsl.2005.02.029
851 Claude-Ivanaj, C., Bourdon, B., Allègre, C.J., 1998. Ra–Th–Sr isotope systematics in Grande
852 Comore Island: a case study of plume–lithosphere interaction. Earth Planet. Sci. Lett.
853 164, 99–117. https://doi.org/10.1016/S0012-821X(98)00195-2
854 Coltorti, M., Bonadiman, C., Hinton, R.W., Siena, F., Upton, B.G.J., 1999. Carbonatite
855 metasomatism of the oceanic upper mantle: evidence from clinopyroxenes and glasses in
856 ultramafic xenoliths of Grande Comore, Indian Ocean. J. Petrol. 40, 133–165.
857 https://doi.org/10.1016/j.epsl.2014.04.027
858 Condamine, P., Médard, E., 2014. Experimental melting of phlogopite-bearing mantle at 1
859 GPa: Implications for potassic magmatism. Earth Planet. Sci. Lett. 397, 80–92.
860 https://doi.org/10.1016/j.epsl.2014.04.027
861 Couch, S., Sparks, R.S.J., Carroll, M.R., 2001. Mineral disequilibrium in lavas explained by
862 convective self-mixing in open magma chambers. Nature 411, 1037–1039.
863 https://doi.org/10.1038/35082540
864 Courgeon, S., Jorry, S.J., Jouet, G., Camoin, G., BouDagher-Fadel, M.K., Bachèlery, P.,
865 Caline, B., Boichard, R., Révillon, S., Thomas, Y., 2017. Impact of tectonic and
866 volcanism on the Neogene evolution of isolated carbonate platforms (SW Indian Ocean).
867 Sediment. Geol. 355, 114–131. https://doi.org/10.1016/j.sedgeo.2017.04.008
868 Daly, R.A., 1925. The geology of Ascension island, in: Proceedings of the American
869 Academy of Arts and Sciences. JSTOR, pp. 3–80.
870 Darnet, M., Wawrzyniak, P., Tarits, P., Hautot, S., D’Eu, J.F., 2020. Mapping the geometry of
871 volcanic systems with magnetotelluric soundings: Results from a land and marine
872 magnetotelluric survey performed during the 2018–2019 Mayotte seismovolcanic crisis.
873 J. Volcanol. Geotherm. Res. 406, 107046.
874 https://doi.org/10.1016/j.jvolgeores.2020.107046

875 Dautria, J.M., Girod, M., Rahaman, O., 1983. The upper mantle beneath eastern Nigeria:
876 inferences from ultramafic xenoliths in Jos and Biu volcanics. J. African Earth Sci. 1,
877 331–338.
878 Debeuf, D., 2004. Étude de l'évolution volcano-structurale et magmatique de Mayotte
879 (archipel des Comores, océan Indien). Université de la Reunion.
880 Deniel, C., 1998a. Geochemical and isotopic (Sr, Nd, Pb) evidence for plume–lithosphere
881 interactions in the genesis of Grande Comore magmas (Indian Ocean). Chem. Geol. 144,
882 281–303. https://doi.org/10.1016/S0009-2541(97)00139-3
883 Deniel, C., 1998b. Geochemical and isotopic (Sr, Nd, Pb) evidence for plume–lithosphere
884 interactions in the genesis of Grande Comore magmas (Indian Ocean). Chem. Geol. 144,
885 281–303. https://doi.org/10.1016/S0009-2541(97)00139-3
886 Dofal, A., Fontaine, F.R., Michon, L., Barruol, G., Tkalcic, H., 2018. Crustal structure
887 variation across the southwestern Indian Ocean from receiver functions determined at
888 Ocean-Bottom Seismometers, in: AGU Fall Meeting 2018. AGU.
889 Dziewonski, A.M., Chou, T., Woodhouse, J.H., 1981. Determination of earthquake source
890 parameters from waveform data for studies of global and regional seismicity. J.
891 Geophys. Res. Solid Earth 86, 2825–2852.
892 Ekström, G., Nettles, M., Dziewoński, A.M., 2012. The global CMT project 2004–2010:
893 Centroid-moment tensors for 13,017 earthquakes. Phys. Earth Planet. Inter. 200, 1–9.
894 Emerick, C.M., Duncan, R.A., 1982. Age progressive volcanism in the Comores Archipelago,
895 western Indian Ocean and implications for Somali plate tectonics. Earth Planet. Sci. Lett.
896 60, 415–428. https://doi.org/10.1016/0012-821X(82)90077-2
897 Famin, V., Michon, L., Bourhane, A., 2020. The Comoros archipelago: a right-lateral
898 transform boundary between the Somalia and Lwandle plates. Tectonophysics 789,
899 228539. https://doi.org/10.1016/j.tecto.2020.228539
900 Feuillet, N., 2019. MAYOBS1 cruise, RV Marion Dufresne.
901 https://doi.org/10.17600/18001217
902 Feuillet, N., Jorry, S., Rinnert, E., Thinon, I., Fouquet, Y., 2019. MAYOBS cruises, RV
903 Marion Dufresne. https://doi.org/10.18142/291
904 Feuillet, N., Jorry, S.J., Crawford, W., Deplus, C., Thinon, I., Jacques, E., Saurel, J.M.,
905 Lemoine, A., Paquet, F., Satriano, C., Aiken, C., Foix, O., Kowalski, P., Laurent, A.,
906 Rinnert, E., Cathalot, C., Donval, J.P., Guyader, V., Gaillot, A., Scalabrin, C., Moreira,
907 M., PelRer, A., Beauducel, F., Grandin, R., Ballu, V., Daniel, R., Pelleau, P., Gomez, J.,
908 Besançon, S., Geli, L., Bernard, P., Bachelery, P., Fouquet, Y., BerRl, D., Lemarchand,

A., Woerd, J. Van der, 2021. Birth of a large volcanic edifice through lithosphere-scale diking offshore Mayotte (Indian Ocean). EarthArXiv. https://doi.org/10.31223/X5B89P

Flower, M.F.J., 1973. Evolution of basaltic and differentiated lavas from Anjouan, Comores Archipelago. Contrib. to Mineral. Petrol. 38, 237–260.

Flower, M.F.J., 1972. Petrology of volcanic rocks from Anjouan, Comores Archipelago. Bull. Volcanol. 36, 238–250.

Fouquet, Y., Feuillet, N., 2019. MAYOBS4 cruise, RV Marion Dufresne. https://doi.org/10.17600/18001238

Fujimaki, H., 1986. Partition coefficients of Hf, Zr, and REE between zircon, apatite, and liquid. Contrib. to Mineral. Petrol. 94, 42–45.

Ghiorso, M.S., Gualda, G.A.R., 2015. An H 2 O–CO 2 mixed fluid saturation model compatible with rhyolite-MELTS. Contrib. to Mineral. Petrol. 169, 1–30. https://doi.org/10.1007/s00410-015-1141-8

Ghiorso, M.S., Sack, R.O., 1995. Chemical mass transfer in magmatic processes IV. A revised and internally consistent thermodynamic model for the interpolation and extrapolation of liquid-solid equilibria in magmatic systems at elevated temperatures and pressures. Contrib. to Mineral. Petrol. 119, 197–212. https://doi.org/10.1007/BF00307281

Giehl, C., Marks, M., Nowak, M., 2013. Phase relations and liquid lines of descent of an iron-rich peralkaline phonolitic melt: an experimental study. Contrib. to Mineral. Petrol. 165, 283–304.

Grant, T.B., Milke, R., Pandey, S., Jahnke, H., 2013. The Heldburg Phonolite, Central Germany: Reactions between phonolite and xenocrysts from the upper mantle and lower crust. Lithos 182, 86–101. https://doi.org/10.1016/j.lithos.2013.09.012

Grove, T.L., Donnelly-Nolan, J.M., 1986. The evolution of young silicic lavas at Medicine Lake Volcano, California: Implications for the origin of compositional gaps in calc-alkaline series lavas. Contrib. to Mineral. Petrol. 92, 281–302. https://doi.org/10.1007/BF00572157

Gualda, G.A.R., Ghiorso, M.S., Lemons, R. V, Carley, T.L., 2012. Rhyolite-MELTS: a modified calibration of MELTS optimized for silica-rich, fluid-bearing magmatic systems. J. Petrol. 53, 875–890. https://doi.org/10.1093/petrology/egr080

Hajash, A., Armstrong, R.L., 1972. Paleomagnetic and radiometric evidence for the age of the Comores Islands, west central Indian Ocean. Earth Planet. Sci. Lett. 16, 231–236. https://doi.org/10.1016/0012-821X(72)90195-1

943 Irving, A.J., Price, R.C., 1981. Geochemistry and evolution of Iherzolite-bearing phonolitic
944 lavas from Nigeria, Australia, East Germany and New Zealand. Geochim. Cosmochim.
945 Acta 45, 1309–1320. https://doi.org/10.1016/0016-7037(81)90224-6
946 Jochum, K.P., Weis, U., Schwager, B., Stoll, B., Wilson, S.A., Haug, G.H., Andreae, M.O.,
947 Enzweiler, J., 2016. Reference values following ISO guidelines for frequently requested
948 rock reference materials. Geostand. Geoanalytical Res. 40, 333–350.
949 https://doi.org/10.1111/j.1751-908X.2015.00392.x
950 Jorry, S.J., 2019. MAYOBS2 cruise, RV Marion Dufresne.
951 https://doi.org/10.17600/18001222
952 Klemme, S., Günther, D., Hametner, K., Prowatke, S., Zack, T., 2006. The partitioning of
953 trace elements between ilmenite, ulvospinel, armalcolite and silicate melts with
954 implications for the early differentiation of the moon. Chem. Geol. 234, 251–263.
955 https://doi.org/10.1016/j.chemgeo.2006.05.005
956 Kyle, P.R., Moore, J.A., Thirlwall, M.F., 1992. Petrologic evolution of anorthoclase phonolite
957 lavas at Mount Erebus, Ross Island, Antarctica. J. Petrol. 33, 849–875.
958 https://doi.org/doi.org/10.1093/petrology/33.4.849
959 Laporte, D., Lambart, S., Schiano, P., Ottolini, L., 2014. Experimental derivation of nepheline
960 syenite and phonolite liquids by partial melting of upper mantle peridotites. Earth Planet.
961 Sci. Lett. 404, 319–331. https://doi.org/10.1093/petroj/40.1.133
962 Le Bas, M.J., Streckeisen, A.L., 1991. The IUGS systematics of igneous rocks. J. Geol. Soc.
963 London. 148, 825–833.
964 Le roex, A.P., Cliff, R.A., Adair, B.J.I., 1990. Tristan da Cunha, South Atlantic: geochemistry
965 and petrogenesis of a basanite-phonolite lava series. J. Petrol. 31, 779–812.
966 https://doi.org/10.1093/petrology/31.4.779
967 Lemoine, A., Briole, P., Bertil, D., Roullé, A., Foumel, M., THINON, I., Raucoules, D.,
968 Michele, M. de, Valty, P., 2020. The 2018-2019 seismo-volcanic crisis east of Mayotte,
969 Comoros islands: seismicity and ground deformation markers of an exceptional
970 submarine eruption. https://doi.org/10.31223/osf.io/d46xj
971 Loges, A., Schultze, D., Klügel, A., Lucassen, F., 2019. Phonolitic melt production by
972 carbonatite Mantle metasomatism: evidence from Eger Graben xenoliths. Contrib. to
973 Mineral. Petrol. 174, 93. https://doi.org/10.1007/s00410-019-1630-2
974 Ludden, J.N., 1977. The mineral chemistry and origin of xenoliths from the lavas of Anjouan,
975 Comores Archipelago, western Indian Ocean. Contrib. to Mineral. Petrol. 64, 91–107.
976 Luhr, J.F., Carmichael, I.S.E., Varekamp, J.C., 1984. The 1982 eruptions of El Chichón

977 Volcano, Chiapas, Mexico: mineralogy and petrology of the anhydritebearing pumices.
978 J. Volcanol. Geotherm. Res. 23, 69–108. https://doi.org/10.1016/0377-0273(84)90057-X
979 Mahood, G.A., Stimac, J.A., 1990. Trace-element partitioning in pantellerites and trachytes.
980 Geochim. Cosmochim. Acta 54, 2257–2276. https://doi.org/10.1016/0016-
981 7037(90)90050-U
982 Marks, M., Markl, G., 2003. Ilímaussaq 'en miniature': closed-system fractionation in an
983 agpaitic dyke rock from the Gardar Province, South Greenland (contribution to the
984 mineralogy of Ilímaussaq no. 117). Mineral. Mag. 67, 893–919.
985 https://doi.org/10.1180/0026461036750150
986 Matsui, Y., Onuma, N., Nagasawa, H., Higuchi, H., Banno, S., 1977. Crystal structure control
987 in trace element partition between crystal and magma. Bull. Minéralogie 100, 315–324.
988 McDonough, W.F., Sun, S.-S., 1995. The composition of the Earth. Chem. Geol. 120, 223–
989 253. https://doi.org/https://doi.org/10.1016/0009-2541(94)00140-4
990 Michon, L., 2016. The volcanism of the Comoros archipelago integrated at a regional scale,
991 in: Active Volcanoes of the Southwest Indian Ocean. Springer, pp. 333–344.
992 https://doi.org/10.1007/978-3-642-31395-0_21
993 Moussallam, Y., Oppenheimer, C., Scaillet, B., Kyle, P.R., 2013. Experimental phase-
994 equilibrium constraints on the phonolite magmatic system of Erebus Volcano,
995 Antarctica. J. Petrol. 54, 1285–1307. https://doi.org/10.1093/petrology/egt012
996 Nash, W.P., Carmichael, I.S.E., Johnson, R.W., 1969. The mineralogy and petrology of
997 Mount Suswa, Kenya. J. Petrol. 10, 409–439.
998 Neave, D.A., Maclennan, J., Thordarson, T., Hartley, M.E., 2015. The evolution and storage
999 of primitive melts in the Eastern Volcanic Zone of Iceland: the 10 ka Grímsvötn tephra
1000 series (ie the Saksunarvatn ash). Contrib. to Mineral. Petrol. 170, 21.
1001 https://doi.org/10.1007/s00410-015-1170-3
1002 Nehlig, P., Lacquement, F., Bernard, J., Caroff, M., Deparis, J., Jaouen, T., Pelleter, A.A.,
1003 Perrin, J., Prognon, C., Vittecoq, B., 2013. Notice de la carte géologique de Mayotte.
1004 BRGM/RP-61803-FR, 135 p., 45 ill., 1 ann.
1005 Nougier, J., Cantagrel, J.M., Karche, J.P., 1986. The Comores archipelago in the western
1006 Indian Ocean: volcanology, geochronology and geodynamic setting. J. African Earth Sci.
1007 5, 135–144. https://doi.org/10.1016/0899-5362(86)90003-5
1008 Pelleter, A.-A., Caroff, M., Cordier, C., Bachèlery, P., Nehlig, P., Debeuf, D., Arnaud, N.,
1009 2014. Melilite-bearing lavas in Mayotte (France): An insight into the mantle source
1010 below the Comores. Lithos 208, 281–297. https://doi.org/10.1016/j.lithos.2014.09.012

1011 Price, R.C., Green, D.H., 1972. Lherzolite nodules in a “mafic phonolite” from north-east
1012 Otago, New Zealand. Nat. Phys. Sci. 235, 133–134.
1013 https://doi.org/10.1038/physci235133a0
1014 Prowatke, S., Klemme, S., 2006. Trace element partitioning between apatite and silicate
1015 melts. Geochim. Cosmochim. Acta 70, 4513–4527.
1016 Putirka, K.D., 2008. Thermometers and Barometers for Volcanic Systems. Rev. Mineral.
1017 Geochemistry 69, 61–120. https://doi.org/10.2138/rmg.2008.69.3
1018 Reubi, O., Blundy, J., 2009. A dearth of intermediate melts at subduction zone volcanoes and
1019 the petrogenesis of arc andesites. Nature 461, 1269–1273.
1020 https://doi.org/10.1038/nature08510
1021 ReVoSiMa, 2021. Bulletin n°21 de l’activité sismo-volcanique à Mayotte, du 1 au 31 janvier
1022 2021. https://doi.org/ISSN : 2680-1205
1023 Romano, P., Scaillet, B., White, J.C., Andújar, J., Di Carlo, I., Rotolo, S.G., 2020.
1024 Experimental and thermodynamic constraints on mineral equilibrium inpantelleritic
1025 magmas. Lithos 376, 105793. https://doi.org/10.1016/j.lithos.2020.105793
1026 Rutherford, M.J., 1969. An experimental determination of iron biotite-alkali feldspar
1027 equilibria. J. Petrol. 10, 381–408.
1028 Scaillet, B., Pichavant, M., Cioni, R., 2008. Upward migration of Vesuvius magma chamber
1029 over the past 20,000 years. Nature 455, 216–219. https://doi.org/10.1038/nature07232
1030 Schiano, P., Bourdon, B., Clocchiatti, R., Massare, D., Varela, M.E., Bottinga, Y., 1998.
1031 Low-degree partial melting trends recorded in upper mantle minerals. Earth Planet. Sci.
1032 Lett. 160, 537–550. https://doi.org/10.1016/S0012-821X(98)00109-5
1033 Schnetzler, C.C., Philpotts, J.A., 1970. Partition coefficients of rare-earth elements between
1034 igneous matrix material and rock-forming mineral phenocrysts—II. Geochim.
1035 Cosmochim. Acta 34, 331–340. https://doi.org/10.1016/0016-7037(70)90110-9Get
1036 Späth, A., Roex, A.P. Le, Duncan, R.A., 1996. The geochemistry of lavas from the Comores
1037 Archipelago, Western Indian Ocean: petrogenesis and mantle source region
1038 characteristics. J. Petrol. 37, 961–991. https://doi.org/10.1093/petrology/37.4.961
1039 Stamps, D.S., Kreemer, C., Fernandes, R., Rajaonarison, T.A., Rambolamanana, G., 2021.
1040 Redefining East African Rift System kinematics. Geology.
1041 Stix, J., Gorton, M.P., 1990. Variations in trace element partition coefficients in sanidine in
1042 the Cerro Toledo Rhyolite, Jemez Mountains, New Mexico: Effects of composition,
1043 temperature, and volatiles. Geochim. Cosmochim. Acta 54, 2697–2708.
1044 Strong, D.F., 1972. Petrology of the island of Moheli, western Indian Ocean. Geol. Soc. Am.

Bull. 83, 389–406.
Tatsumi, Y., Suzuki, T., 2009. Tholeiitic vs calc-alkalic differentiation and evolution of arc crust: constraints from melting experiments on a basalt from the Izu–Bonin–Mariana Arc. J. Petrol. 50, 1575–1603. https://doi.org/10.1093/petrology/egp044
Thompson, R.N., Flower, M.F.J., 1971. One-atmosphere melting and crystallization relations of lavas from Anjouan, Comores Archipelago, Western Indian Ocean. Earth Planet. Sci. Lett. 12, 97–107. https://doi.org/10.1016/0012-821X(71)90060-4
Tzevahirtzian, A., Zaragosi, S., Bachèlery, P., Biscara, L., Marchès, E., 2021. Submarine morphology of the Comoros volcanic archipelago. Mar. Geol. 432. https://doi.org/10.1016/j.margeo.2020.106383
Ubide, T., Mollo, S., Zhao, J., Nazzari, M., Scarlato, P., 2019. Sector-zoned clinopyroxene as a recorder of magma history, eruption triggers, and ascent rates. Geochim. Cosmochim. Acta 251, 265–283. https://doi.org/10.1016/j.gca.2019.02.021
Zinke, J., Reijmer, J.J.G., Thomassin, B.A., Dullo, W.-C., Grootes, P.M., Erlenkeuser, H., 2003. Postglacial flooding history of Mayotte lagoon (Comoro archipelago, southwest Indian Ocean). Mar. Geol. 194, 181–196. https://doi.org/10.1016/S0025-3227(02)00705-3

Figures:

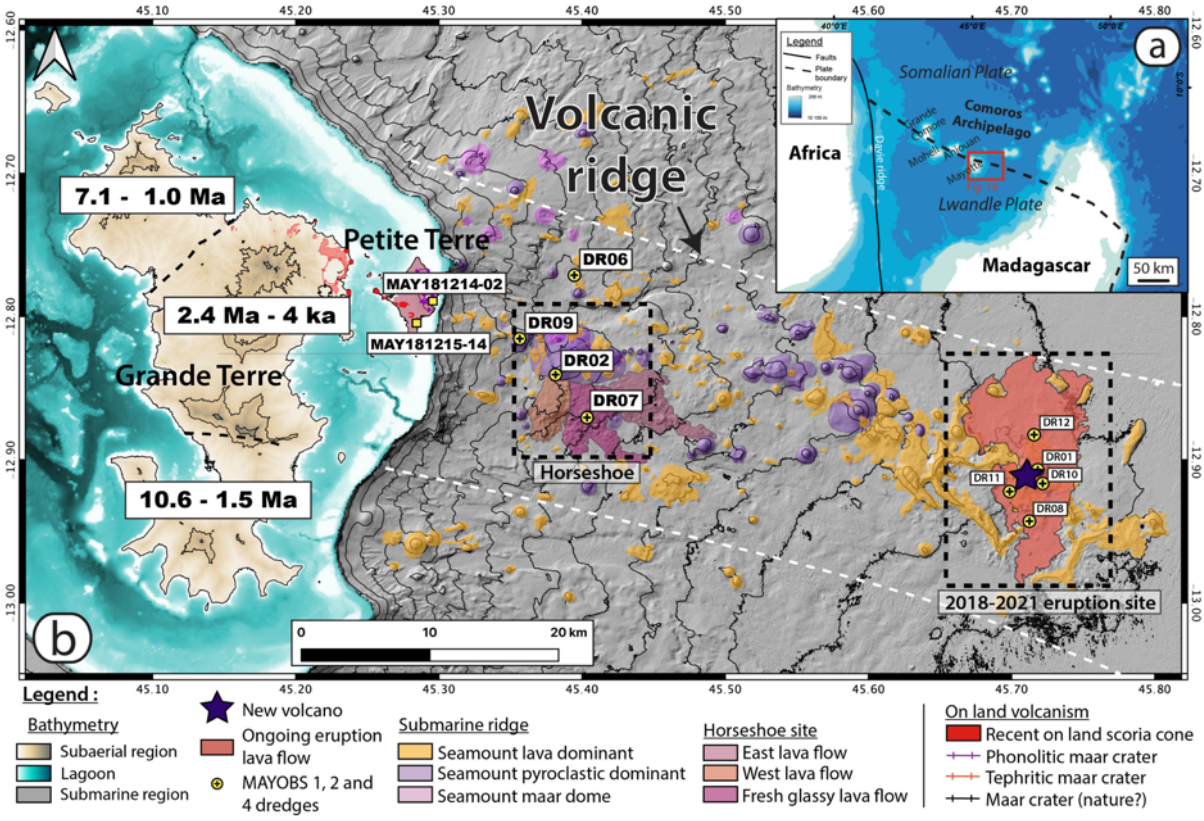

Fig. 1: a) Location of Comoros archipelago in the Mozambique Channel. b) Geological map of the active submarine volcanic ridge showing the location of our samples offshore and on land. Ages are from (Debeuf, 2004; Emerick and Duncan, 1982; Hajash and Armstrong, 1972; Nougier et al. 1986; Pelleter et al. 2014). DR labels correspond to the dredged samples.

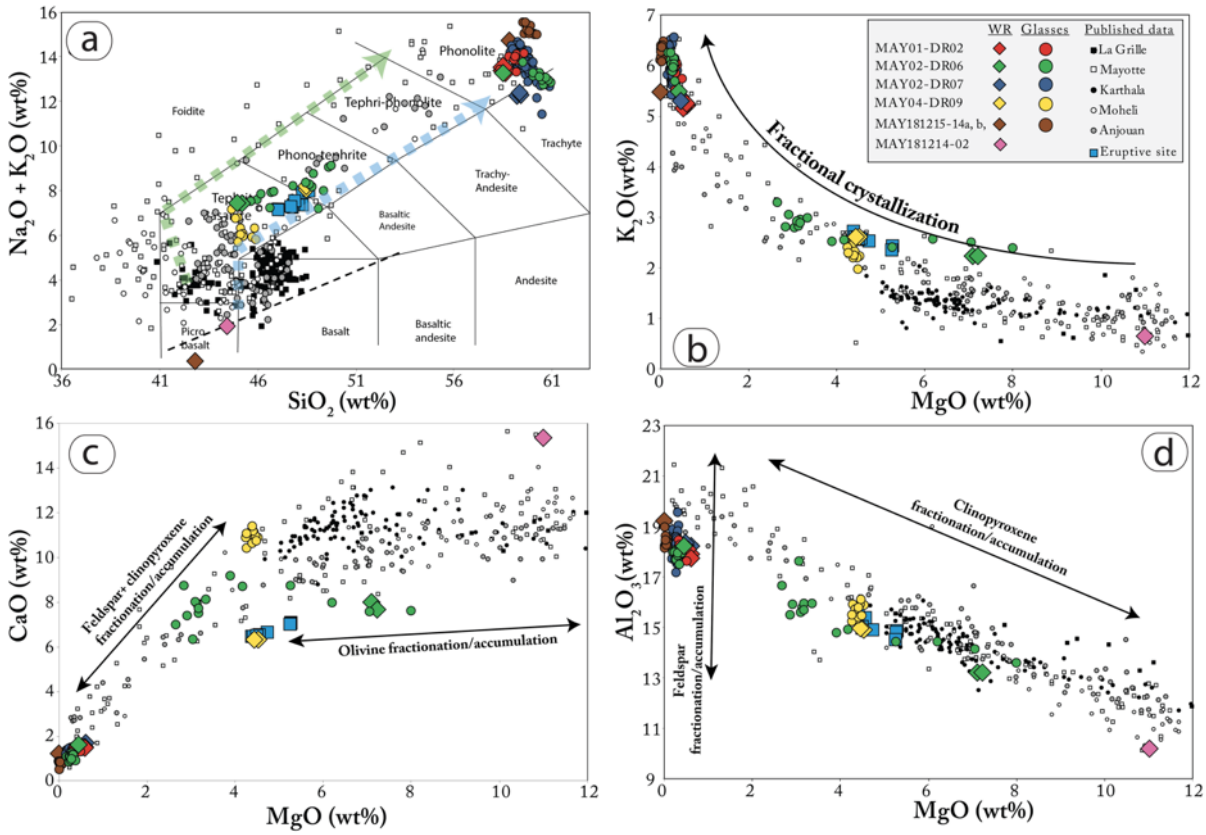

Fig. 2: Geochemical signature of the volcanic ridge east of Mayotte. a) Classification of our samples using the TAS diagram after Le Bas and Streckeisen, (1991), b) FeO vs MgO diagram, c) CaO vs MgO diagram, d) Al_2O_3 vs MgO diagram. Blue arrows and green arrows respectively show the moderately silica-undersaturated (Karthala-type) and the highly silica-undersaturated (La Grille-type) trends for Mayotte lavas (from Bachèlery & Hémond 2016). The difference between the two trends is interpreted as the result of decreasing degrees of partial melting. The more silica-undersaturated La Grille lavas (green trend) may have been produced by relatively small degrees of partial melting of a garnet lherzolite mantle source at depths about 80 km, whereas the moderately alkalic Karthala series (blue trend) reflects larger degrees of partial melting of a similar garnet lherzolite or spinel lherzolite source (Späth et al.1996; Bachèlery & Hémond 2016).

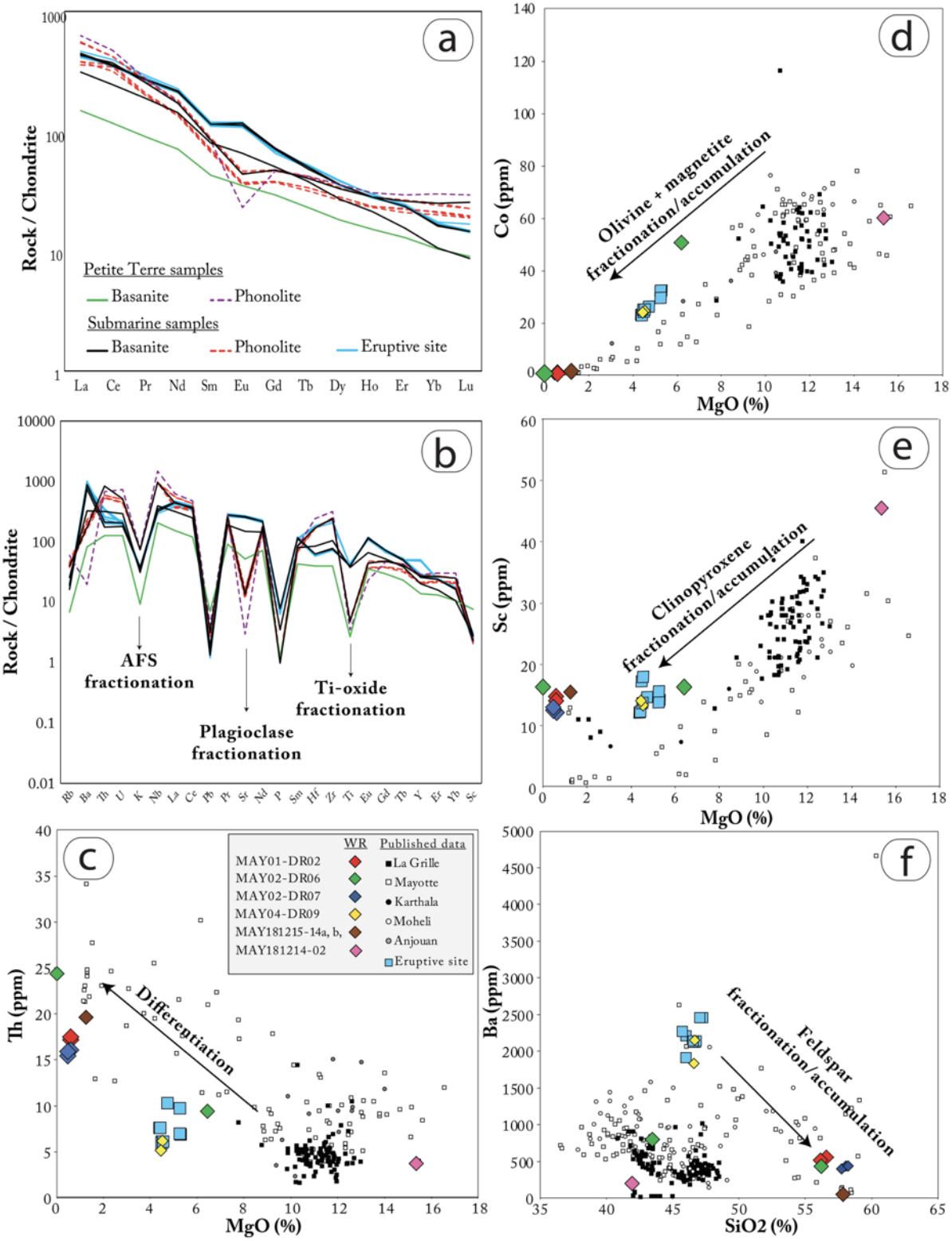

Fig. 3: Trace element variations in basanites and phonolites samples. a) Chondrite- normalized REE patterns, b) Spider diagrams of incompatible trace elements normalized to primitive mantle concentrations (McDonough and Sun, 1995), c) V vs Th diagram, d) Co vs MgO diagram, e) Sc vs MgO diagram, and f) Ba vs SiO_2 diagram.

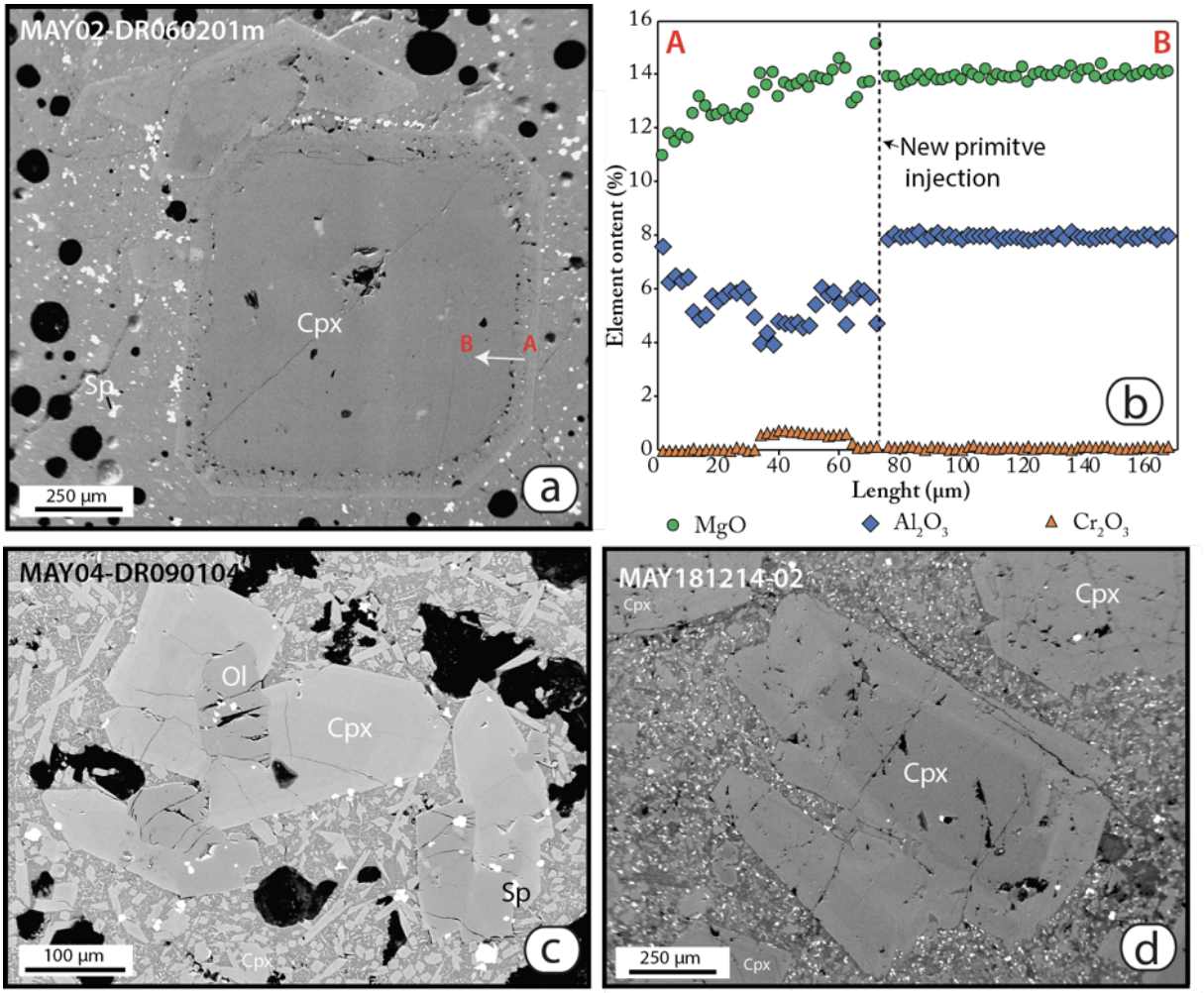

Fig. 4: Textural and petrological features of basanite lavas sampled offshore on the submarine volcanic ridge; a) BSE image of a zoned clinopyroxene crystal in sample MAY02-DR060201m, b) MgO, Al_2O_3 and Cr_2O_3 concentrations along the profile drawn on a), c) BSE image of a glomerocryst in dredged sample MAY04-DR090104, and d) BSE image of a zoned clinopyroxene crystal in Petite Terre Island sample (MAY181214-02).

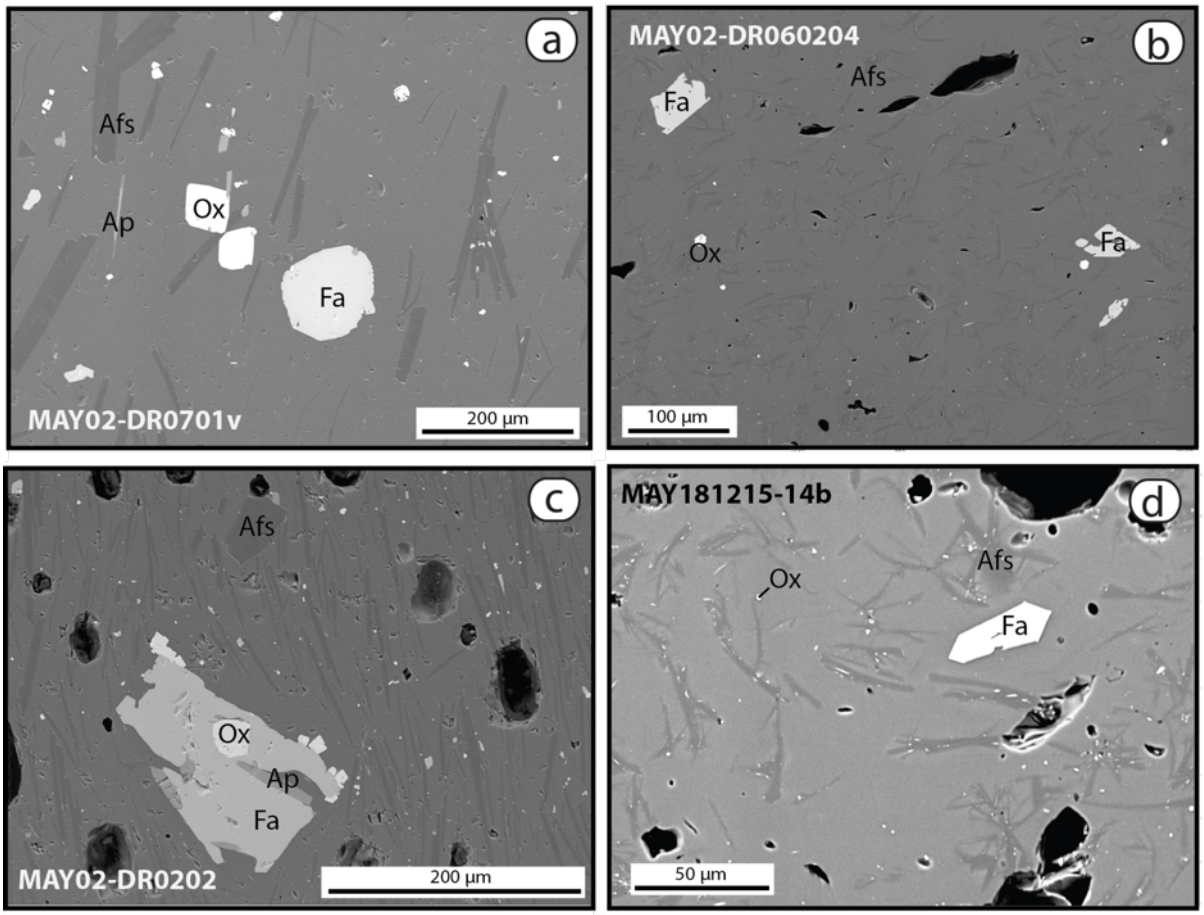

Fig. 5: Textural and petrological features of phonolite lavas sampled offshore on the active submarine volcanic ridge; BSE images of dredged samples a) MAY02-DR0701v, b) MAY02-DR060204, c) MAY01-DR0202, and d) BSE images of Petite Terre Island sample (MAY181215-14b). Phonolites have a trachytic texture with laths of alkali feldspar (Afs), and skeletal to subhedral olivine (Fa) microphenocrysts intergrown with apatite (Ap) and oxide (Ox).

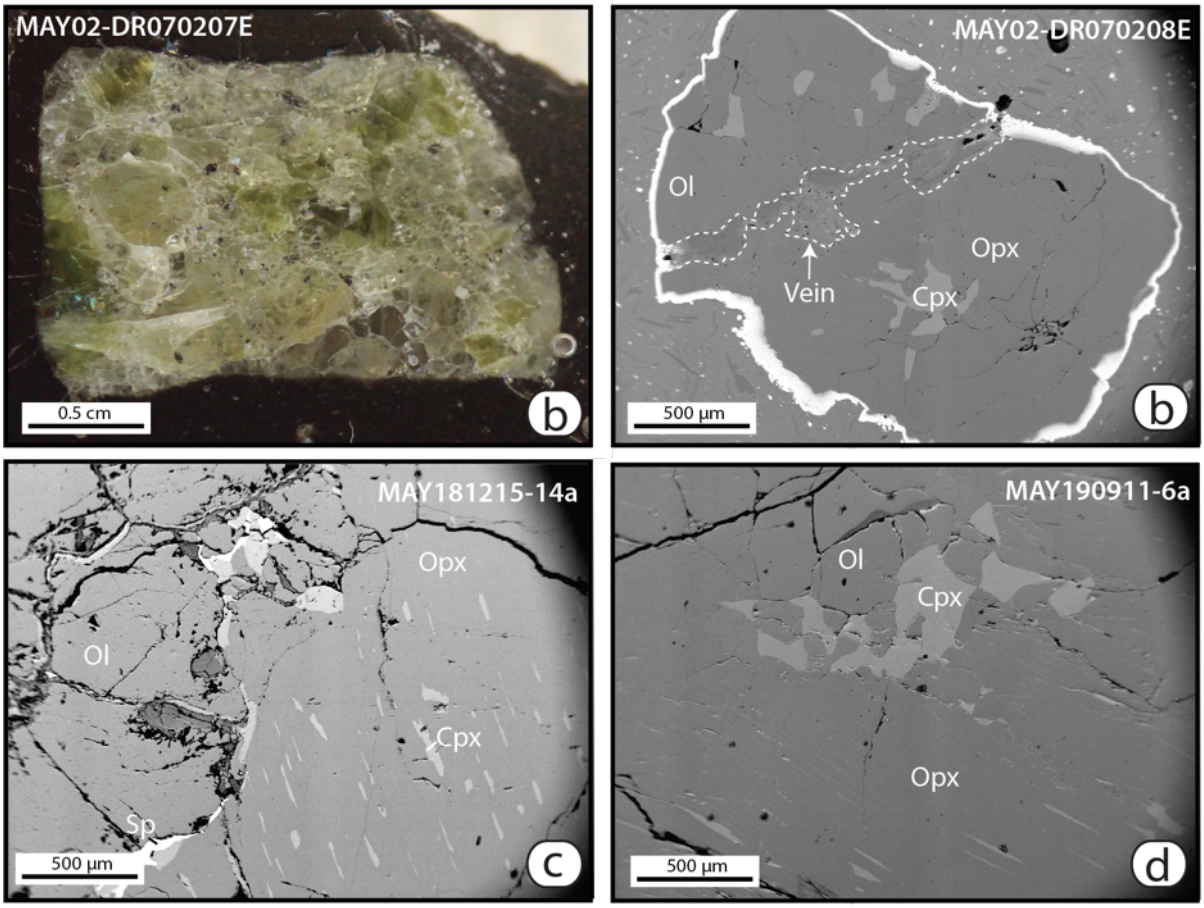

Fig. 6: Textural and petrological features of mantle xenoliths in phonolites lavas: a) picture of mantle xenolith in phonolite; BSE images of samples b) MAY02-DR070208E, c) MAY181215-14a, and d) MAY190911-6a containing large olivine and orthopyroxene crystals and smaller clinopyroxene and spinel crystals. The reaction rims mostly formed of bright fayalite-rich olivine crystals are prominent in b).

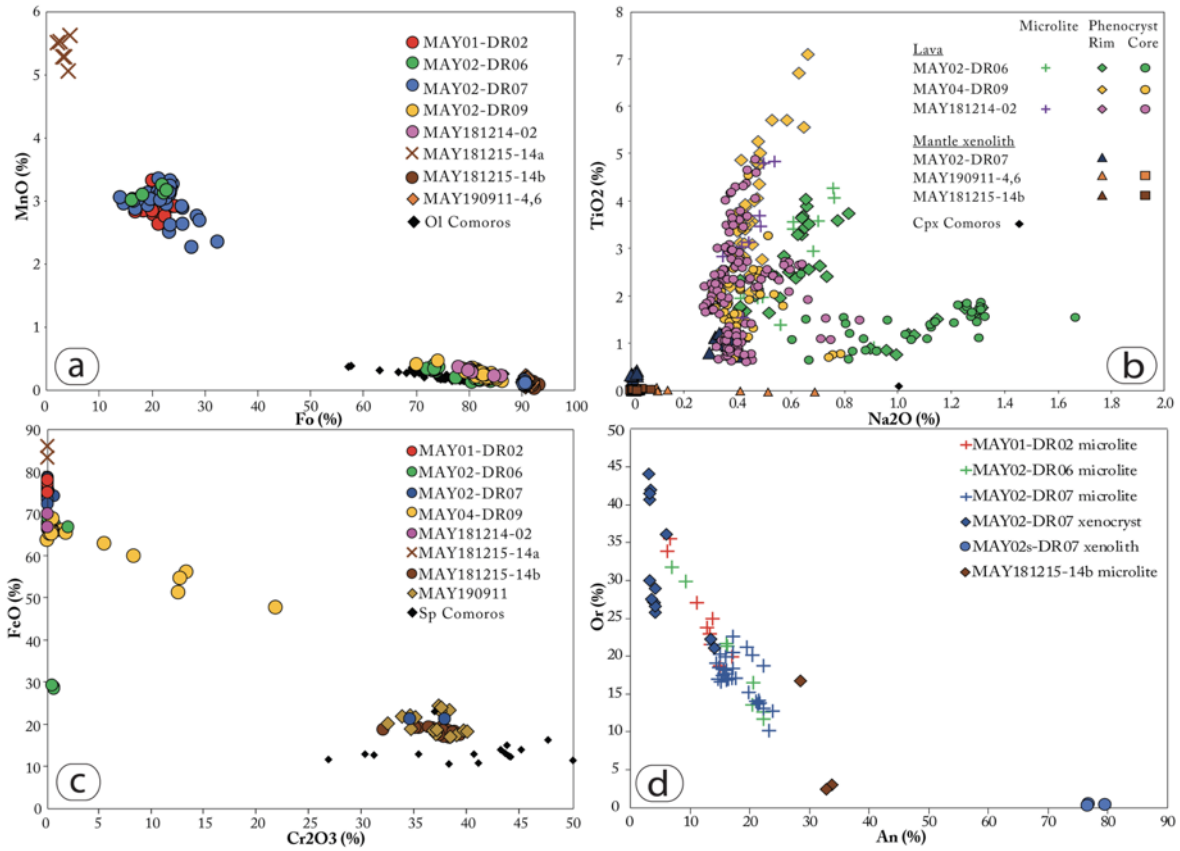

Fig. 7: Mineral compositions analyzed in the sampled rocks. a) olivine, b) clinopyroxene and orthopyroxene, c) Fe-Ti oxides, d) feldspar. Our data are compared to minerals in Comoros lavas (Coltorti et al. 1999; Flower, 1972; Ludden, 1977; Schiano et al. 1998; Späth et al. 1996). The two parallel clinopyroxene trends correspond to sector zoning.

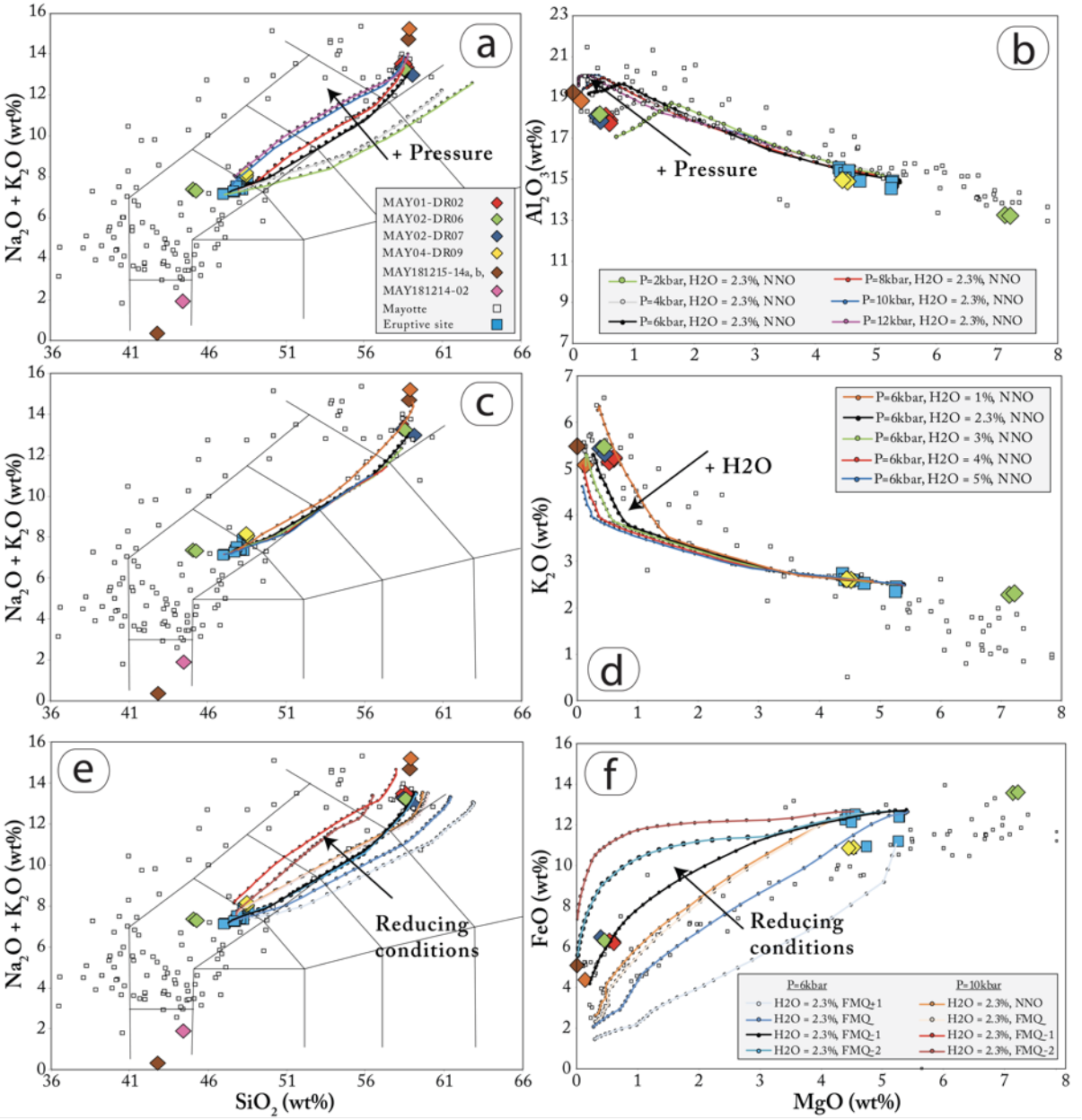

Fig. 8: Rhyolite-MELTS models using MAY01-DR0105 basanite as parental magma. Models were run to test if the phonolites can be derived by deep fractional crystallization of the basanites. For each model, temperature decreases from 1200 to 700 °C, with a 10 °C step. We tested a-b) a range of possible pressures from 0.2 to 1.2 GPa, c-d) H_2O concentrations from 1.0 wt% to 5.0 wt%, and e-f) a range of oxygen fugacities buffered at FMQ+1, NNO~FMQ+0.5, FMQ, FMQ-1 and FMQ-2.

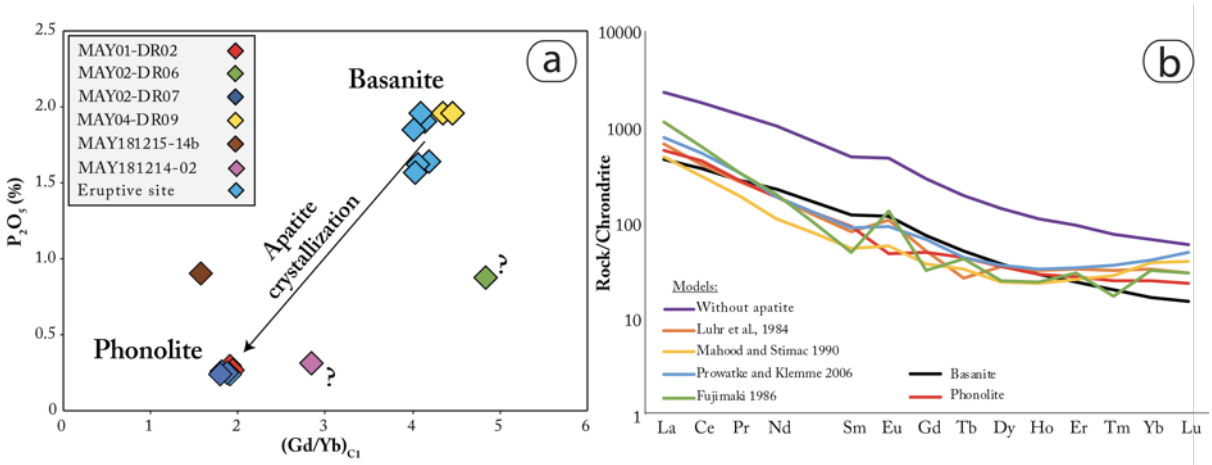

Fig. 9: Nature and depth of the source of the active submarine ridge magmas. REE elements could indicate two different sources for basanitic and phonolitic magmas. However, we suggest that REE element contents are impacted by apatite crystallization. b) Model REE patterns obtained by 80% fractional crystallization of a cumulate containing 3-4 wt% apatite (assuming REEs are perfectly incompatible in all other phases) using different partition coefficients for REEs in apatite (Fujimaki, 1986; Luhr et al. 1984; Mahood and Stimac, 1990; Prowatke and Klemme, 2006) compared with measured REE patterns for phonolite and basanite magmas.

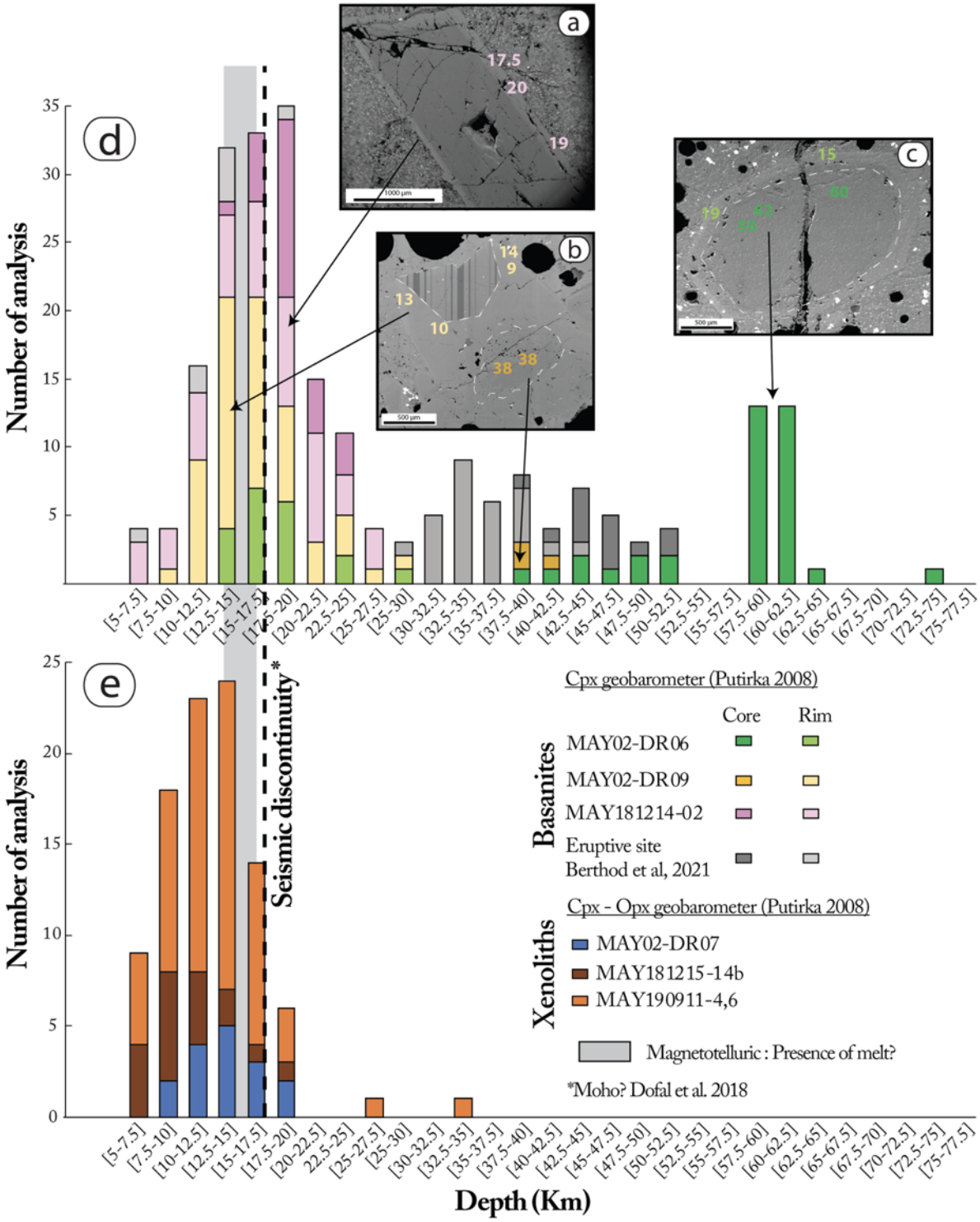

Fig. 10: Histograms showing geobarometry estimations using a-d) zoned clinopyroxene phenocrysts geobarometry and e) clinopyroxene-orthopyroxene pairs in the mantle xenoliths Our results are compared to magnetotelluric interpretation (presence of melt, Darnet et al. 2020). Zoned clinopyroxene barometry is from equation 32a of (Putirka, 2008, Supplementary Tab. 8), which has a typical error of 0.28 GPa (9 km). Clinopyroxene/Orthopyroxene barometry in mantle xenoliths is from equation (38) of Putirka (2008), Supplementary Tab. 9.

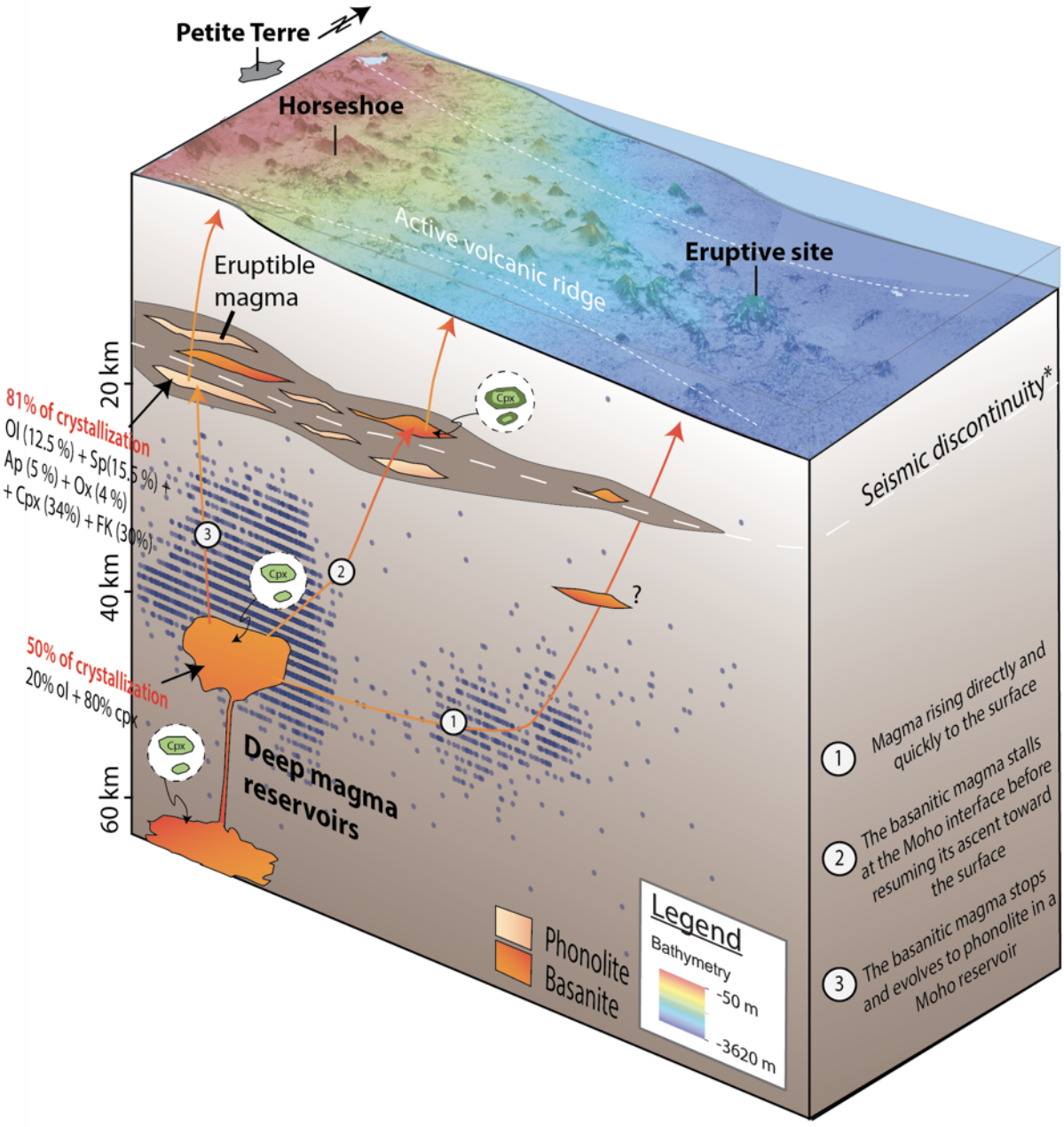

Fig. 11: Cartoon illustrating the magmatic system feeding the active volcanic ridge of Mayotte. The magma forms between 80 – 100 km depth and then rises until it reaches deep magma chambers (< 35 km). Using whole-rock geochemistry, Berthod et al. (2021) suggested that the magma have undergone fifty percent of crystallization in these reservoirs (twenty percent of olivine and eighty percent of clinopyroxene). Following an internal or external trigger, the eruption begins, and magma rises to the surface. From this stage, we propose three scenarios: In the first scenario the magma rises directly and quickly to the surface generating the aphanitic basanites (Berthod et al. 2021). In the second, the basanitic magma stalls at the Moho interface before resuming its ascent toward the surface. Finally, in the last scenario the basanitic magma stops and the depth of the Moho and evolves to phonolite with 81% of crystallization

(anorthoclase (30%), olivine (12.5 %), magnetite (15.5 %), apatite (5 %), ilmenite (4 %) and clinopyroxene (34 %)) in a Moho reservoir. * Dofal et al. (2018). Blue dots : seismic activity (10.18715/IPGP.2021.kq136bzh)

Table Captions:

Tab. 1: Dredges and on land sample's locations